NAVAL POSTGRADUATE SCHOOL

MONTEREY, CALIFORNIA

THESIS

THREE-DIMENSIONAL DISCRETE ELEMENT MODELING OF FIRST-YEAR SEA ICE RIDGES

by

Travis J. Davis

June 2019

Thesis Advisor:	Timour Radko
Co-Advisor:	Andrew F. Roberts
Second Reader:	Adrian Turner, Los Alamos National Laboratory

THIS PAGE INTENTIONALLY LEFT BLANK

REPORT DOCUMENTATION PAGE			*Form Approved OMB No. 0704-0188*

1. AGENCY USE ONLY *(Leave blank)*	**2. REPORT DATE** June 2019	**3. REPORT TYPE AND DATES COVERED** Master's thesis

4. TITLE AND SUBTITLE THREE-DIMENSIONAL DISCRETE ELEMENT MODELING OF FIRST-YEAR SEA ICE RIDGES	**5. FUNDING NUMBERS**
6. AUTHOR(S) Travis J. Davis	
7. PERFORMING ORGANIZATION NAME(S) AND ADDRESS(ES) Naval Postgraduate School Monterey, CA 93943-5000	**8. PERFORMING ORGANIZATION REPORT NUMBER**
9. SPONSORING / MONITORING AGENCY NAME(S) AND ADDRESS(ES) N/A	**10. SPONSORING / MONITORING AGENCY REPORT NUMBER**

11. SUPPLEMENTARY NOTES The views expressed in this thesis are those of the author and do not reflect the official policy or position of the Department of Defense or the U.S. Government.

12a. DISTRIBUTION / AVAILABILITY STATEMENT Approved for public release. Distribution is unlimited.	**12b. DISTRIBUTION CODE** A

13. ABSTRACT (maximum 200 words)

A three-dimensional discrete element model has been developed to investigate the evolution of particular aspects of pressure ridges in thin, first-year, sea ice. The primary goal of this work is to test one facet of recent theoretical advances in the representation of sea ice thickness in Earth System Models that advocates for the introduction of macro-porosity, ϕ_R, to the state space of basin-scale sea ice models. Macro-porosity is caused by cavities between fractured sea ice blocks created during the formation of ridges during convergence of ice floes in the Southern and Arctic Oceans. Previously, sea ice thickness in basin-scale sea ice models has been represented by a real thickness distribution, g(h), but new mathematical derivations suggest that this should be replaced in predictive models with a bivariate distribution, g(h, ϕ_R). In this thesis, a discrete element model of sea ice is described and then used to investigate the evolution of ϕ_R in three-dimensional ridges. Changes in ϕ_R over time are extremely difficult to measure in the Arctic, and therefore this research bridges observational constraints and theoretical assumptions. The final results suggest that, within the constraints of the given discrete element model, a more sudden change in macro-porosity occurs at the initial creation of a ridge than current theory suggests, but thereafter evolution of macro-porosity follows a path similar to what a Coulombic friction model predicts.

14. SUBJECT TERMS discrete element model, sea ice, Arctic, ridge, LAMMPS	**15. NUMBER OF PAGES** 81
	16. PRICE CODE

17. SECURITY CLASSIFICATION OF REPORT	**18. SECURITY CLASSIFICATION OF THIS PAGE**	**19. SECURITY CLASSIFICATION OF ABSTRACT**	**20. LIMITATION OF ABSTRACT**
Unclassified	Unclassified	Unclassified	UU

NSN 7540-01-280-5500 Standard Form 298 (Rev. 2-89) Prescribed by ANSI Std. 239-18

THIS PAGE INTENTIONALLY LEFT BLANK

Approved for public release. Distribution is unlimited.

THREE-DIMENSIONAL DISCRETE ELEMENT MODELING OF FIRST-YEAR SEA ICE RIDGES

Travis J. Davis
Lieutenant, United States Navy
BS, Colorado School of Mines, 2004

Submitted in partial fulfillment of the
requirements for the degree of

MASTER OF SCIENCE IN METEOROLOGY AND PHYSICAL OCEANOGRAPHY

from the

NAVAL POSTGRADUATE SCHOOL
June 2019

Approved by: Timour Radko
Advisor

Andrew F. Roberts
Co-Advisor

Adrian Turner
Second Reader

Peter C. Chu
Chair, Department of Oceanography

THIS PAGE INTENTIONALLY LEFT BLANK

ABSTRACT

A three-dimensional discrete element model has been developed to investigate the evolution of particular aspects of pressure ridges in thin, first-year, sea ice. The primary goal of this work is to test one facet of recent theoretical advances in the representation of sea ice thickness in Earth System Models that advocates for the introduction of macro-porosity, ϕ_R, to the state space of basin-scale sea ice models. Macro-porosity is caused by cavities between fractured sea ice blocks created during the formation of ridges during convergence of ice floes in the Southern and Arctic Oceans. Previously, sea ice thickness in basin-scale sea ice models has been represented by a real thickness distribution, g(h), but new mathematical derivations suggest that this should be replaced in predictive models with a bivariate distribution, g(h, ϕ_R). In this thesis, a discrete element model of sea ice is described and then used to investigate the evolution of ϕ_R in three-dimensional ridges. Changes in ϕ_R over time are extremely difficult to measure in the Arctic, and therefore this research bridges observational constraints and theoretical assumptions. The final results suggest that, within the constraints of the given discrete element model, a more sudden change in macro-porosity occurs at the initial creation of a ridge than current theory suggests, but thereafter evolution of macro-porosity follows a path similar to what a Coulombic friction model predicts.

THIS PAGE INTENTIONALLY LEFT BLANK

Table of Contents

List of Figures

List of Tables

THIS PAGE INTENTIONALLY LEFT BLANK

List of Acronyms and Abbreviations

USN	U.S. Navy
LAMMPS	Large-Scale Atomic/Molecular Massively Parallel Simulator
DEM	discrete element model
VP	non-linear viscous plastic rheology
AIDJEX	Arctic Ice Dynamics Joint Experiment
DEMSI	Discrete Element Model for Sea Ice
SNL	Sandia National Laboratories
LANL	Los Alamos National Laboratory
CNO	Chief of Naval Operations
ESM	earth system model
DESIgn	Discrete-Element Bonded-Particle Sea Ice Model
VWF	volume weighting function
NSIDC	National Snow and Ice Data Center

THIS PAGE INTENTIONALLY LEFT BLANK

Acknowledgments

First, I must thank Dr. Roberts for his dedication to me in the execution of this research. Without your guidance and outstanding professionalism, I don't think I could have finished this project. I can't thank you enough, and I sincerely hope that I will have the honor of working with you again in the future. Thank you.

Dr. Radko, and the rest of the NPS Oceanography department, thank you for your support. I appreciate every single time you allowed me to vent, or brainstorm, or even brag when I finally managed a modest breakthrough. You have all been so patient and generous with your time. Thank you.

Finally, none of this would have been possible without my wife, Erica. You are the light of my life and without your support, none of this would have been possible. You picked up the slack while I obsessed over code and made these last few years the happiest of my life. The time has flown by, but we have great memories, a beautiful daughter, and I could not be more proud of you. Erica, I love you so much. Thank you.

THIS PAGE INTENTIONALLY LEFT BLANK

CHAPTER 1:
Introduction

Polar sea ice is a thin, Kwok and Cunningham (2008) estimate mean sea ice thickness in the Arctic to be 2-2.5 m, layer of frozen sea water that is found at the ocean-atmosphere interface of the Arctic and Southern Oceans. This ice forms as sea water freezes during the winter and moves in response to the whims of atmospheric and oceanic currents. In the arctic, sea ice covers roughly 7 million km^2, summer minimum, to 14 million km^2, the winter maximum, and shows strong inter-annual variability (Cavalieri and Parkinson 2012). This ice extent, though, measured as the area of open water covered by at least 15% of sea ice, is retreating. Cavalieri and Parkinson (2012) shows that Arctic sea ice is retreating at approximately -51.5 thousand km^2 yr^{-1} (-4.1% $decade^{-1}$), indicating the sensitivity of this ice cover to the warming climate. As shown in Figure 1.1, the National Snow and Ice Data Center (NSIDC) show this trend in sea ice extent retreat is closer to -2.6% $decade^{-1}$.

This retreat represents a significant change to the Arctic climate. One of the mechanisms for this change is the changing Arctic Ocean sea ice albedo, or the ability of the Arctic Ocean to reflect sun light. Sea ice albedo plays an important role in climate regulation through the ice-albedo feedback mechanism (Perovich and Richter-Menge 2009). During the northern hemisphere summer, the albedo of the Arctic serves to reduce the absorption of solar radiation by reflecting a portion of the incoming radiation back into the atmosphere, and thereafter space. Melting of perennial, or thick multi-year, Arctic sea ice, is causing the pack to become more sensitive to small changes in atmospheric temperature (Perovich and Richter-Menge 2009). This transition to thin, first-year, sea ice in the Arctic is reducing the total albedo of the Arctic as more of the Arctic Ocean becomes sea ice free in summer and with the reduction, its ability to reflect incoming solar radiation during the peak solar period. This reduction in the Arctic's ability to reflect solar radiation leads to increased temperatures in the Arctic, which in turn will enhance the retreat of Arctic sea ice. This positive feedback mechanism must be properly accounted for in global climate models to accurately predict the changing climate.

In addition to the ice-albedo feedback mechanism, there are a number of other thermodynamic processes which contribute to the response of the pack to the changing Arctic climate

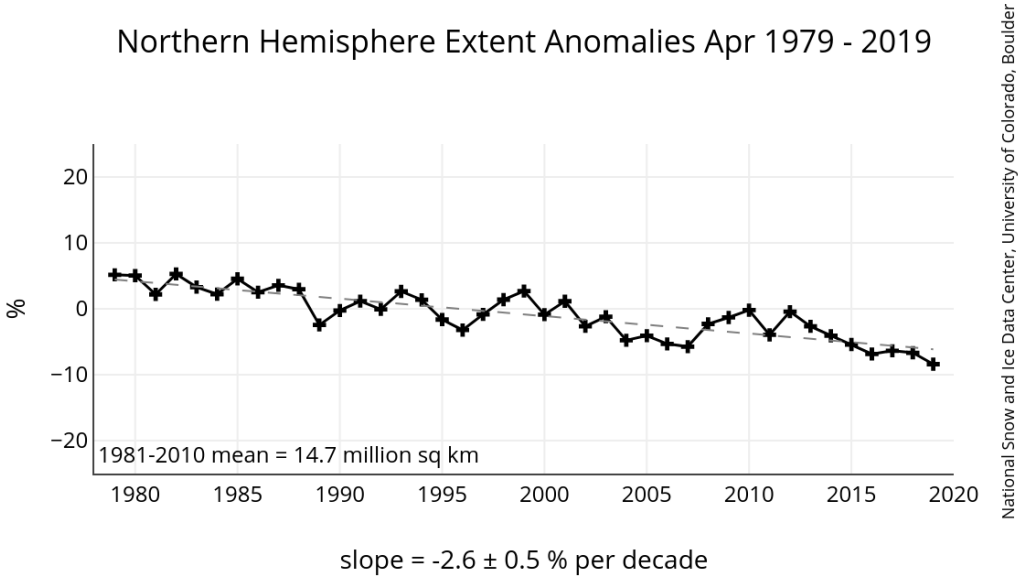

The monthly sea ice anomaly for the northern hemisphere shows a strong negative trend showing a trend of sea ice loss in the Arctic. Accessed 22 May 2019 from https://nsidc.org/data/seaice_index.

Figure 1.1. NSIDC Monthly Sea Ice Extent Anomaly

that are not discussed in this work; thermal conductivity of snow cover and brine pocket inclusion melt rate dependence, for example. In addition to these thermodynamic factors, there are other mechanisms which serve to modify the pack. Sea ice responds dynamically to the motion of the ocean and atmosphere on whose interface it exists. The relative motion of these two bodies of fluid serve to force the sea ice to deform and flex in response. Hutchings et al. (2009) show the distribution of these deformation zones in the Arctic and demonstrate that this deformation is highly localized. This focusing of deformation creates ridges, under convergence, and leads, under divergence, and are a unique characteristic of sea ice marking an irregular distribution of open ocean and sea ice.

Brassington and Coauthors (2015), in a summary of the development of earth system models (ESMs), highlight the reliance on accurate prediction of the distribution of sea ice mass to model the Earth's climate.

1.1 Ridging in Arctic Sea Ice and in Earth System Models

Pressure ridging has long been the subject of study due to its importance in the generation of multi-year sea ice and distribution of sea ice mass in basin scale sea ice simulations. Figure 1.2 shows only the uppermost portion of a ridge, or its sail. Below the ice surface the ridge extends into the water forming a keel that is larger than the sail. The ridge is composed of fractured sea ice rubble, apparent in Figure 1.2, which does not pack as efficiently as the undeformed pack and possesses void regions, or macro-porosity, ϕ_R.

A pressure ridge identified during the Sea Ice Experiment - Dynamic Nature of the Arctic (SEDNA) field expedition. Visible is the sail portion of the ridged ice and the irregular, rubble, generated in the ridging process. Photo courtesy of Andrew Roberts, Los Alamos National Laboratory.

Figure 1.2. In-situ Pressure Ridge. Source: SEDNA (2008).

Campaigns to observe pressure ridges in-situ have provided valuable insight into the basin distribution of sea ice ridges (Davis and Wadhams 1995; Melling and Riedel 1995, 1996; Melling et al. 1993; Wadhams and Davy 1986), pressure ridge morphology (Ekeberg et al. 2015; Johnston and Barker 2000; Strub-Klein and Sudom 2012; Tan and Coauthors 2012; Timco and Burden 1997; Timco et al. 2000; Tucker and Govoni 1981), and the process of

pressure ridge formation (Hopkins 1994, 1998; Weeks 2010; Zubov 1945).

Incorporation of the conclusions and observations made in each of the previous studies have informed sea ice modelers for years. Models developed by Rothrock (1975) and Hibler (1980) were able to predict well the redistribution of sea ice during convergence and the change in mechanical strength of the pack as thicker ice is formed. These models were further improved as research was done on the effect of ridge formation on form drag of ice floes. With the development of a ridge, its sail presents an increasingly large aspect to wind. The increased aspect serves to enhance the pack's response to forcing. Garbrecht et al. (1999) studied the effect of the presence of a single large pressure ridge on the form drag finding that the ridged ice contributes significantly to increased drag in the pack.

Roberts and Coauthors (2019) developed a coarse-grained technique to estimate the distribution of sea ice ridges within a region of strained ice. This effort enables prediction of the compressive strength and mass distribution critical to global sea ice models which are in turn used in fully coupled ESMs. The analytic solution developed, however, is theoretical and requires corroboration. To substantiate the solution presented by Roberts and Coauthors (2019), the model presented in this thesis has been developed to evaluate the development of a pressure ridge in first-year sea ice. This modeling work has been undertaken due to the difficulty in measuring the transition of several state variables during ridging events in real sea ice, including macro-porosity, which is typically evaluated only after a ridge has formed. To allay this observational deficit, the model developed in this thesis generates simulated ridge states which can then be easily compared to the analytic solution recently derived by Roberts and Coauthors (2019).

1.2 U.S. Navy (USN) Relevance

The Arctic is home to millions of people and, established in the Ottawa Declaration of 1996, eight Arctic nations comprising the Arctic Council. This council, of which the United States is a member, represents the diversity of the region and highlights the complexity of Arctic economic and territorial claims. While the council was created to harbor cooperation and effective stewardship in the region, the emergence of Russian adventurism threatens the long-held international order in the Arctic (Secretary of Defense 2018). The eight Arctic nations have complex claims to the region's economic resources. This complexity is typified

by the competing Canadian, Danish, and Russian claims to the north pole. Russia claims the region as an extension of its continental shelf extending from its northern coast while Denmark claims the Lomonosov Ridge, which itself extends across the Arctic and through the north pole (British Broadcasting Corporation 2014; Kramer 2016). With the backdrop of competing territorial claims, an emboldened Russia is seeking to assert its influence in the region. Furthermore, with the retreat of summer sea ice extent, China is seeking to capitalize on the newly open trans-arctic shipping routes that will form the backbone of its "Polar Silk Road" to European markets (Wen 2019).

The U.S. Joint Chiefs of Staff are pivoting their efforts to meeting the threat to the United States from great power competition, specifically the emergence of increased Chinese and Russian belligerence. In Chief of Naval Operations, USN (2018), the Chief of Naval Operations (CNO) outlines the threats to national security posed by these nations. As China and Russia assert influence along critical sea lines of communication, the USN must rise to meet this emerging world order with assertive near-peer competitors. The CNO asserts that Chinese and Russian actions are "frequently confrontational." Shea (2019) discuss the emerging Arctic, with its complex political landscape and untapped bounty, as a region where a potential new Cold War could begin.

According to Melia et al. (2016), the disappearance of multi-year sea ice and the emergence of seasonal (forming in the winter months and melting completely by the end of summer) sea ice coverage in the Arctic is likely to open the region to enhanced commercial utilization, particularly trans-Arctic shipping. Figure 1.3 shows two scenarios and their effect on shipping route availability. The figure shows two climate model simulations; one predicting moderate and the other extreme carbon emissions. The conclude that ships that re not ice-hardened will be able to regularly take the more direct trans-Arctic route within the next 50 years, which until recently has been too dangerous a voyage for them.

Furthermore, Francis and Skific (2015) put forward the idea that as sea ice extent retreats, mid-latitude weather patterns could have become more variable, leading to more extreme weather events. It is this dynamism in the Arctic region that necessitates the development of accurate sea ice prediction tools to support informed decisions on the protection of National interests, resource exploitation operations, and environmental climate prediction. A new generation of global, high resolution, and fully coupled ESMs are under development which

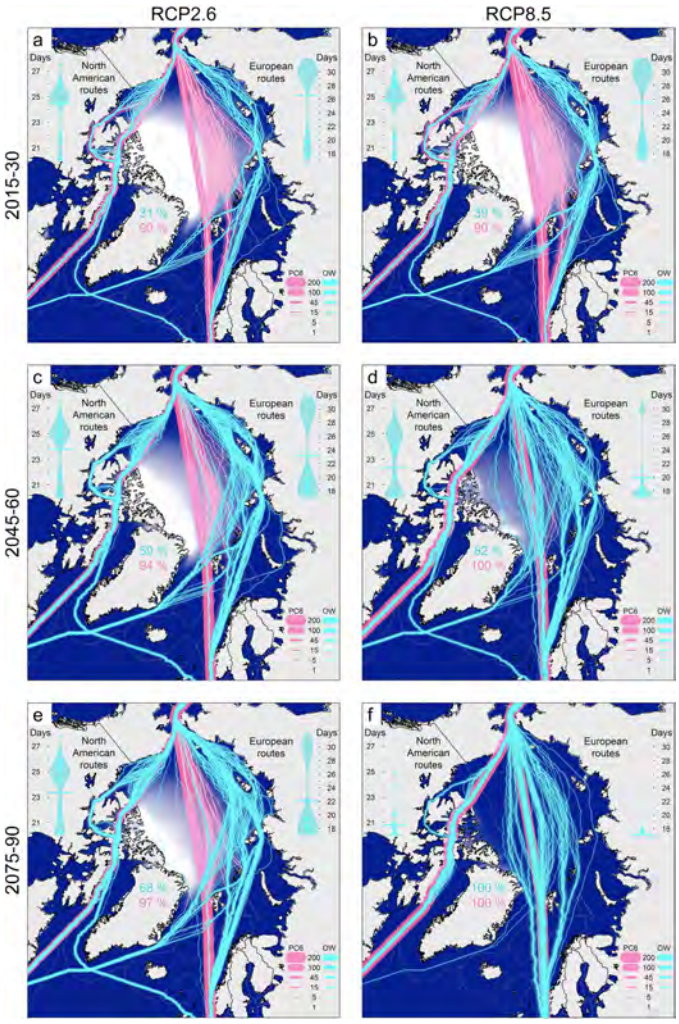

The replacement of multi-year sea ice with seasonal first-year sea ice across the Arctic basin will enable greater access to trans-arctic shipping routes as their shorter distances realize greater cost efficiency in comparison to typical routes through the Suez and Panama canals.

Figure 1.3. Predicted Trans-Arctic Shipping Routes. Source: Melia et al. (2016).

promise to bring better, and more reliable, climate prediction products to decision makers giving the Nation the tools necessary to cope with this new and emerging environment.

1.3 Motivation for Study

Work presented in this thesis complements the creation of the Discrete Element Model for Sea Ice (DEMSI), a new sea ice model developed by Los Alamos National Laboratory (LANL) and Sandia National Laboratories (SNL). At low resolution (approximately 100 km), sea ice behavior is able to be simulated as a continuum material. Models developed by Hibler (1979) and those in its lineage rely on this simplification to solve sea ice dynamics for use in climate models. However, as addressed by Coon et al. (2007), these continuum models are limited by the resolution of the model physics accurate to scales of about 10 km, even if the numerical resolution of the model is much less. Figure 1.4 further illustrates the conclusions reached by Coon et al. (2007). This limitation is at a resolution much lower than is required by the new generation of ESMs, necessitating the development of a new generation of sea ice models. At high resolution sea ice must be modeled using discrete elements (Herman 2016).

DEMSI is currently under development, and when it is complete will use two-dimensional, circular elements that will have an approximate diameter of 1 km. However, at this scale a typical assumption of discrete element models (DEMs), that all elements are rigid, fails. Ridges in sea ice often have a horizontal scale on the order of 1-50 m (Weeks 2010), which is much smaller than the size of an individual DEMSI floe. This scale discrepancy means that the emergent features caused by sea ice convergence are not able to be modeled by the simple rearrangement of the model elements, which may represent collections of floes rather than just individual floes. Therefore, internal yielding of individual elements is required to capture pressure ridging events; a requirement not typically included in basic DEM modeling. To allay this limitation in the model, DEMSI will implement internal element deformation consistent with ridging dynamics outlined in Roberts and Coauthors (2019). While the equations developed by Roberts and Coauthors (2019) are able to generate distributions of sea ice thickness for ridged ice, there is a paucity of observations with which to ensure that the scheme is an accurate representation of ridge states. In order to address the lack of data, the model presented in this thesis has been developed to create a system by which the ridge state distributions can be generated and compared to those produced in the aforementioned theoretical study. The discrete element model developed in this thesis generates virtual ridge states that are created using a three-dimensional, high resolution, granular material that produces ridge features subject only to a defined ridge

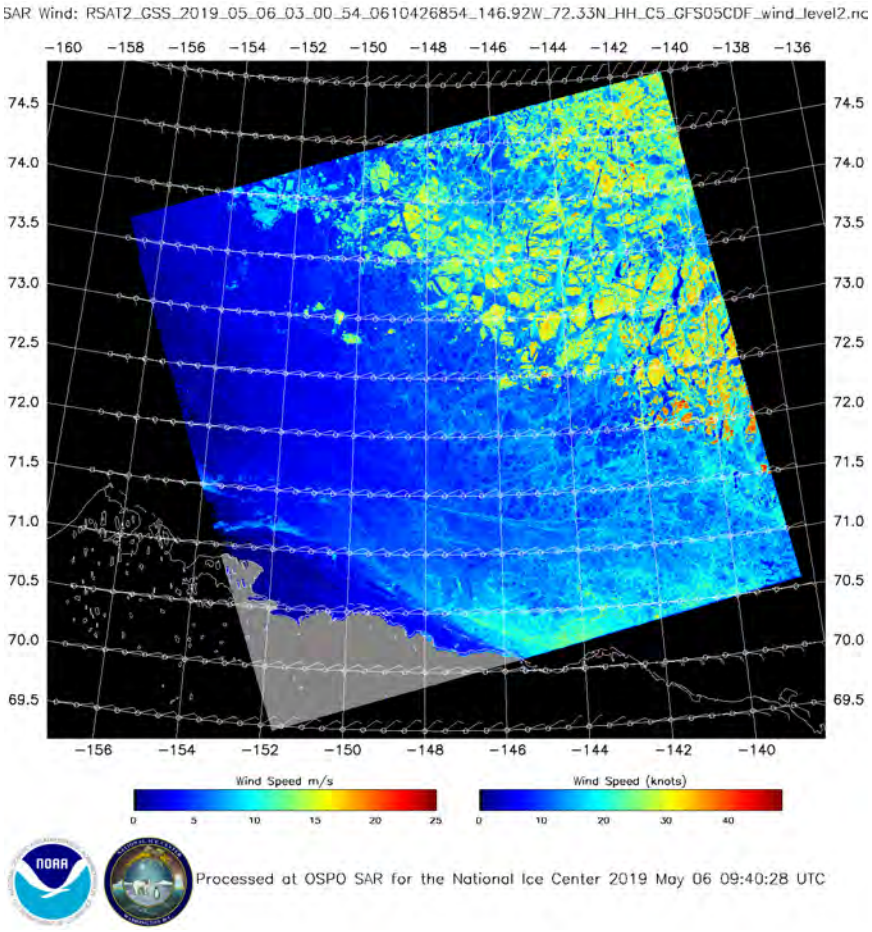

Pictured is the marginal ice zone sea ice near Prudhoe Bay, Alaska. The irregular distribution of floes and their sizes corroborates the conclusions of Coon et al. (2007). In this region and at this resolution, the sea ice is clearly not a continuum material. Reproduced from https://www.ospo.noaa.gov/data/ocean/sar/sarwinds_20190506.html.

Figure 1.4. Visible Irregularity in Arctic Sea Ice

strain, initial spatial distribution of particles, and simple boundary forcing. The model has been developed to extract critical ridge variables, including keel depth, sail height, and macro-porosity distributions as functions of location in space and time within a ridge. The ensuing simulations are compared to the analytic solutions developed by Roberts and Coauthors (2019).

CHAPTER 2:
Background

In pursuit of a theoretically-based approach to thickness redistribution during ridging events, Roberts and Coauthors (2019) developed an analytic solution for the trajectory through ridge state space for sea ice undergoing ridging. Their mathematical solution to the co-evolution of thickness, macro-porosity and strain indicates that the thickness distribution of sea ice, which has historically been a simple distribution of thickness, $g(h)$, must be expanded to include a dependence on macro-porosity, $g(h, \phi_R)$. More information about $g(h)$, and how it is modeled, is available in Thorndike and Coauthors (1975) and Lipscomb and Coauthors (2007). There is, however, little observational data associating ridge thickness with its macro-porosity for use in validating the solution. Data is required that ties the current strain of a ridge, a function of the amount of ice that has been converged into the ridge, and the macro-porosity, and their interrelationship through the entire formation event. Investigation of the evolution of a pressure-ridge from undeformed sea-ice to a mature ridge is difficult to measure. Therefore, the development of a technique to create these ridges in a controlled, easily repeated and modified way has typically been approached with the use of models (Hopkins 1994, 1998; Parmerter and Coauthors 1972).

2.1 Anatomy of a Sea Ice Pressure Ridge

This study follows from previous models of individual ridges, and will focus on the generation of a simulated sea ice pressure ridge from first year sea ice using the discrete element method. Figure 2.1 shows a cross section of an idealized pressure ridge. Apparent in the figure are its sail height, H_s, and its keel depth, H_k. Figure 2.1 shows the primary features of most pressure ridges and serves as the template for algorithms to identify, in the model output, the formed ridge. Pressure ridges form at the boundaries of convergence between two sheets, or floes, of sea ice. This study is limited to the assessment of only first year ice with the two feed sheets of the same thickness, but the general shape is similar for all pressure ridges in this research, as in a large portion of previous ridging studies. Ridging generates sea ice rubble between converging floes. This rubble is the fractured pieces of sea ice that have been broken from the parent sheets and become part of a rubble pile subject to

sideways pressure from the floes and buoyancy due to its density deficit relative to sea water. With continued convergence, more rubble is generated and is forced into the characteristic quasi-triangular ridge shape.

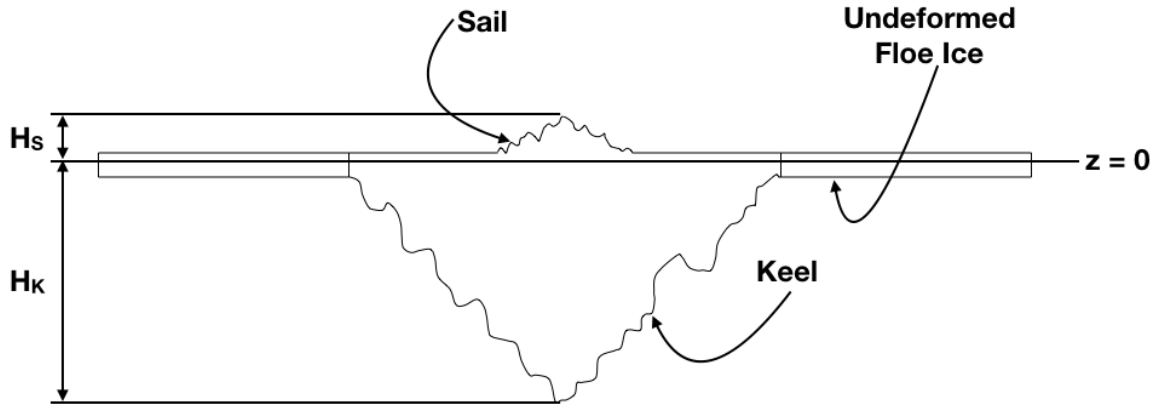

An idealized ridge profile including the undeformed floe ice, sail and keel. The deformed region is characterized by increased macro-porosity and potential energy density. With the measured ridge strain, a function of the total convergence, these three variables define the ridge state. The ridge properties are primarily defined by the sail height, H_s, the keel depth, H_k, and the macro-porosity, ϕ_R.

Figure 2.1. Pressure Ridge Profile Schematic

The keel, or the portion of the ridge beneath the water line, is larger than the sail, the part above the water line, because it is the most efficient conversion of kinetic energy of the converging floes to potential energy stored in the ridge. It takes less work to force a piece of ice rubble beneath the surface of the water than it does to force the same piece of rubble above the water line. The macro-porosity, ϕ_R, of this ridge state is the fraction of void space in the rubble region of the ridge and represents a critical, missing, component to dynamic sea ice models. Porous sea ice ridges are less resilient to melting because of their increased surface area exposed to water and air and occupy more volume thus increasing their cross section for aerodynamic and hydrodynamic drag than if $\phi_R = 0$.

2.2 Basin Scale Continuum Sea Ice Models

Early sea-ice modeling work done by Coon and Coauthors (1974), in conjunction with the Arctic Ice Dynamics Joint Experiment (AIDJEX), created an early sea ice model

that treated sea ice as a continuous elastic-plastic solid. The elastic-plastic assumption states that the floe interactions can be modeled by two types of deformation: those that occur at a stress state within the plastic deformation envelope and those that occur on the plastic deformation envelope. Deformations that occur within are elastic and are therefore reversible. Conversely, those that occur on the envelope are plastic or completely irreversible and permanent. It is in these permanent deformations that the model developed in Coon and Coauthors (1974) addressed ridging and cracking of sea ice.

Under convergent conditions, and at the failure limit, the ice becomes thicker. Equation 2.1, from Lipscomb and Coauthors (2007), describes the evolution of the sea ice thickness distribution. The rate of change in the distribution is dependent upon three factors. The first term on the right-hand side is the convergence of the ice, the second term is the change in thickness due to melt and thaw by thermodynamic processes, and the final term is a mechanical redistribution term. This treatment of sea ice thickness evolution in time enables the development of realistic sea ice extent and thickness distributions across the Arctic, further allowing for a more rigorous treatment of thermodynamic and dynamic processes affecting the Arctic climate system. At the core of continuum type models that simulate sea ice deformation on ocean basin scales, are the conservation of momentum, a constitutive law, an ice thickness distribution evolution relationship, and an ice strength equation to solve for sea ice dynamics and continuity (Hibler 1979).

$$\frac{\partial g}{\partial t} = -\nabla \cdot (\mathbf{u} g) - \frac{\partial}{\partial h}(f g) + \psi \tag{2.1}$$

The momentum balance solves for the material acceleration (or deceleration) of sea ice due to contributions by the Coriolis force, atmospheric drag stress, oceanic drag stress, sea surface height gradient, and internal forces within the ice. Application of Newton's second law yields

$$m\frac{D\mathbf{u}}{Dt} = -mf\mathbf{k} \times \mathbf{u} + \boldsymbol{\tau}_a + \boldsymbol{\tau}_w - mg\nabla H + \mathbf{F} \tag{2.2}$$

where,

$$\boldsymbol{\tau}_a = c_a \rho_a |\mathbf{U}_a| (\mathbf{U}_a \cos\phi + \mathbf{k} \times \mathbf{U}_a \sin\phi) \tag{2.3}$$

and

$$\boldsymbol{\tau}_w = c_w \rho_w |\mathbf{U}_w - \mathbf{u}|[(\mathbf{U}_w - \mathbf{u})\cos\theta + \mathbf{k} \times (\mathbf{U}_w - \mathbf{u})\sin\theta]. \tag{2.4}$$

For definitions of the symbols used in Equation 2.2, and those following, see Table 2.1.

The final term in the equation, $\mathbf{F} = \nabla \cdot \sigma$, requires a constitutive law to relate the internal forces to the stress state of the material, σ_{ij}. Coon and Coauthors (1974) used an elastic-plastic constitutive law wherein any stress states that occur within the yield curve are elastic and those occurring on the yield curve are plastic.

Table 2.1. Symbol Definitions for Continuum Dynamics Equations

m	mass per unit area	$\mathbf{u}$	ice velocity
σ_{ij}	internal stress tensor	H	dynamic sea surface height
$\boldsymbol{\tau}_w$	ocean stress vector	$\boldsymbol{\tau}_a$	wind stress vector
$\mathbf{U}_w$	geostrophic ocean current	$\mathbf{U}_a$	geostrophic wind
$\mathbf{F}$	Internal Force ($\nabla \cdot \sigma$)	$\dot{\epsilon}_{ij}$	strain rate tensor
η	shear viscosity	ζ	bulk viscosity
e	elliptic yield curve eccentricity	P	Pressure
δ_{ij}	Kronecker Delta	i, j	tensor indices (1,2)

While the justification for this assumption is well defended, it leads to the unfortunate aspect of the AIDJEX era model in which strains are effectively stored indefinitely to reverse elastic deformations. Hibler (1979) notes that this is a computational inefficiency that leads to the model being ineffective for long time scale (climatology) modeling.

To address this, and other computational concerns, Hibler (1979) developed a sea ice model based on a similar continuum assumption. However, he made the further assumption that the ice has no elastic deformation mode, but rather deforms as a highly viscous material undergoing plastic deformation. This assumption removed the requirement to store strains indefinitely and allowed for even greater simplification. By making the viscous-plastic assumption, the model approximates sea ice as a slowly creeping fluid over top the ocean. This type of flow is parameterized by confining the local stress states within the modeled

sea ice to an elliptic yield curve where the nonlinear bulk and shear viscosities, ζ and η, respectively, are dependent on the local strain rate, $\dot{\epsilon}_{ij}$, through the following relationships:

$$\sigma_{ij} = 2\eta\dot{\epsilon}_{ij} + (\zeta - \eta)\dot{\epsilon}_{kk}\delta_{ij} - \frac{P\delta_{ij}}{2} \tag{2.5}$$

where, $\zeta = P/2\Delta$, $\eta = P/2\Delta e^2$, and

$$\Delta = \sqrt{\left(\dot{\epsilon}_{11}^2 + \dot{\epsilon}_{22}^2\right)(1 + e^{-2}) + e^{-2}\dot{\epsilon}_{12}^2 + 2\dot{\epsilon}_{11}\dot{\epsilon}_{22}(1 - e^{-2})}. \tag{2.6}$$

Equations 2.5 and 2.6 are functions of the local strain rate tensor, $\dot{\epsilon}_{ij}$, indicating that the internal stress state is itself a function of the tensile and shear modes of deformation and are proportional to the rates at which the material is deforming. These relationships produce the characteristic elliptic yield curve of Hibler's model, see Figure 2.2. For comparison, a Newtonian viscous fluid yield curve is also included to demonstrate the difference in the ability of the non-linear viscous plastic rheology (VP) and Newtonian material to sustain stresses at equilibrium.

From these equations, the zonal (x) and meridional (y) internal force components are computed as

$$F_x = \frac{\partial}{\partial x}\left[(\eta + \zeta)\frac{\partial u}{\partial x} + (\zeta - \eta)\frac{\partial v}{\partial y} - \frac{P}{2}\right] + \frac{\partial}{\partial y}\left[\eta\left(\frac{\partial u}{\partial y} + \frac{\partial v}{\partial x}\right)\right] \tag{2.7}$$

and

$$F_y = \frac{\partial}{\partial y}\left[(\eta + \zeta)\frac{\partial v}{\partial y} + (\zeta - \eta)\frac{\partial u}{\partial x} - \frac{P}{2}\right] + \frac{\partial}{\partial x}\left[\eta\left(\frac{\partial u}{\partial y} + \frac{\partial v}{\partial x}\right)\right]. \tag{2.8}$$

The rheology of the material though, is highly dependent on the local mechanical characteristics of the sea ice. The VP model assumes that it is largely a function of sea ice thickness and uses simple mass conservation arguments to develop the thickness distribution on which η and ζ are based. This formulation is a simple model tuning factor reliant on an isotropic

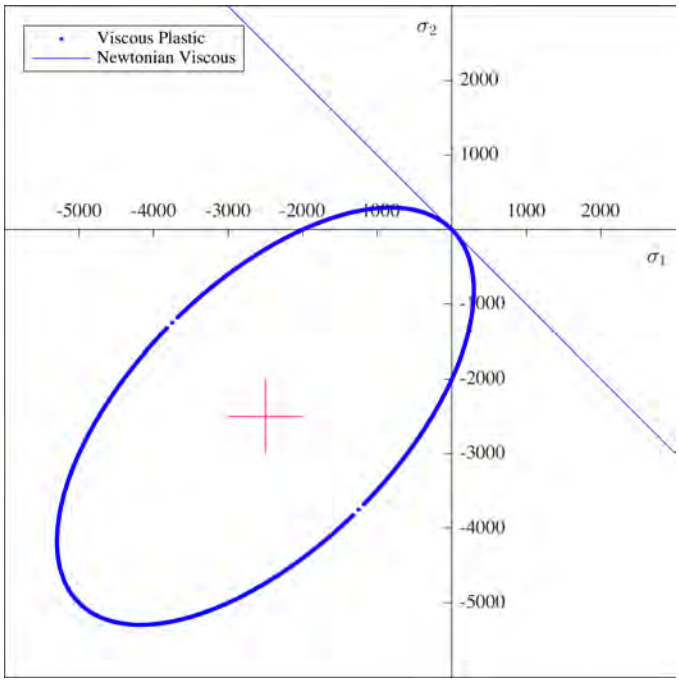

Presentation of the principal stress states (σ_1, σ_2), as derived from equations presented in Hibler, 1979, produced for a Viscous Plastic Rheology. The figure shows the full set of potential stress states the VP material is sustaining dependent upon the local strain rate tensor.

Figure 2.2. Elliptic Yield Curve for Viscous Plastic Rheology

assumption and has little physical basis.

2.3 Sea Ice Anisotropy

While significant computational improvements have been made to continuum sea ice models allowing for gains in model resolution, this lineage of modeling still assumes that sea ice is isotropic. The isotropic assumption allows for the treatment of sea ice as a homogenous material with variable spatial extent. Many of the unique characteristics of sea ice, its motion and spatial variability particularly, owe their existence to sea ice's severe anisotropy. Figure 2.3 shows an aerial view of typical sea ice cover showing clearly the consistent orientations of faults in the material. Isotropic materials do not have preferred failure orientations. However, sea ice, an anisotropic material, clearly fails along preferred orientations. As sea ice model resolution has improved, the isotropic limitation of AIDJEX era models has been addressed in a number of novel ways. Most of this work has been done by

attempting to parameterize at sub-grid scales the anisotropy's effect on the modeled grid-scale motions and behaviors of the sea ice. Wilchinsky et al. (2011) included effects on the pack from sea ice fault reorientation. Tsamados et al. (2013) accounted for the orientation and configuration of sea ice elements. Tsamados and Coauthors (2014) parameterized the pack's environmental drag characteristics due to ridge and lead formation.

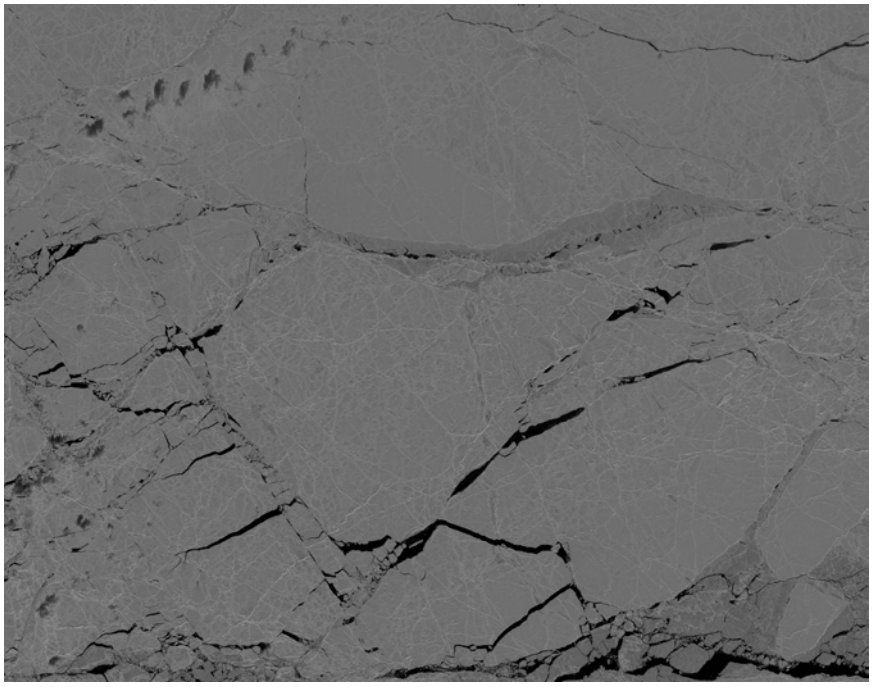

Pictured is an aerial photograph of sea ice. The apparent preferential orientation of fractures generated in the ice field show the inapplicability of the isotropic assumption to high resolution sea ice modeling. Reproduced from https://gfl.usgs.gov/gallery_main.shtml?current=4.

Figure 2.3. Visible Anisotropy in Arctic Sea Ice

Each of these techniques seek to accomplish the same goal, parameterize a continuum model to modify the behavior to be more consistent with real ice. For instance, Tsamados and Coauthors (2014) seek to parameterize the highly anisotropic distribution of ridges and leads within grid cells. The environmental drag coefficients in equations 2.3 and 2.4 are highly dependent on boundary layer roughness and require precise estimations of the ridge state of a sea ice grid point to accurately model the dynamics of the system. The technique outlined in Tsamados and Coauthors (2014) develops more representative environmental momentum flux by including variations in the ice roughness allowing for better simulations

of sea ice dynamics. However, these parameterizations ultimately are attempts to extend the life of models developed with limited computational capability and adherence to continuum modeling schemes for sea ice. The modifications included previously provide valuable insight into the behavior of sea-ice. However, these parameterizations tend to constrain the system and dissuade the development of emergent mechanical features of the pack.

2.4 Discrete Element Sea Ice Models

An alternative to the parameterization schemes discussed in Section 2.3 is to model the sea ice system in such a way as to allow for the anisotropy to evolve naturally due to deterministic pair interactions at small scales. DEMs simulate highly complex macroscopic behavior through simple pair-wise interactions between a collection of rigid small-scale particles. These small-scale particle dynamics are then constrained through fundamental relationships and the system is allowed to evolve. These models are uniquely suited to highly anisotropic systems and are computationally efficient at sufficient levels of processing parallelism and small temporal and spatial scales.

An example DEM sea ice model, developed by Herman (2016), is the Discrete-Element Bonded-Particle Sea Ice Model (DESIgn) which is two-dimensional. The dynamics of this model are defined for the i^{th} element of the system. N.B.: From this point forward in this thesis i and j will exclusively refer to the i^{th} and j^{th} elements in a DEM. Definitions of the terms used in the following equations are given in Table 2.2.

Like their continuum model counterparts, DEM models begin with a basic dynamics equation governing the motion of the sea ice elements,

$$m_i \frac{d\mathbf{u}_i}{dt} = -m_i f \mathbf{k} \times \mathbf{u}_i + \int_{S_i} \check{\mathbf{f}}_{s,i} ds + \int_{V_i} \check{\mathbf{f}}_{b,i} dv + \sum_{j \in C_i(t)} \hat{\mathbf{F}}_{ij,n} \tag{2.9}$$

where the rate of change of the i^{th} element momentum is due to the Coriolis force, the surface force, the body force, and the sum of contact Forces.

Unlike continuum models, where vorticity is computed from the curl of the velocity field, DEMs require explicit treatment of angular momentum,

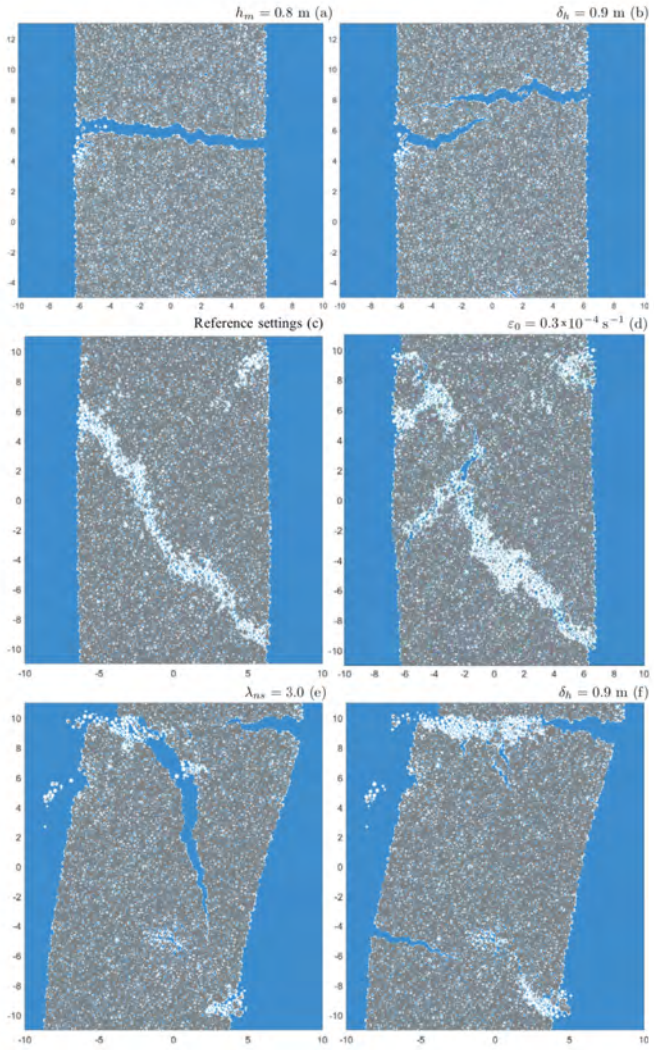

An example of a DEM simulating the failure of plates of modeled sea ice under prescribed strain rates. Figure adapted from Herman (2016).

Figure 2.4. DESIgn Simulation Example of a Discrete Element Model. Source: Herman (2016).

$$m_i \frac{r_i^2}{2} \frac{d\omega_i}{dt} = \mathbf{k} \cdot \left(\int_{S_i} \mathbf{r} \times \mathbf{f}_{s,i} ds + \int_{V_i} \mathbf{r} \times \mathbf{f}_{b,i} dv + \sum_{j \in C_i(t)} \mathbf{r}_{ij} \times \hat{\mathbf{F}}_{ij,t} \right) \tag{2.10}$$

where the rate of change of the i^{th} elements angular momentum, assuming the elements

are cylindrical ($I = \frac{r_i^2}{2}$), is defined normal to the surface and is the cumulative effect of the tangential components of the forces acting on the element.

Table 2.2. Symbol Definitions for DEM Dynamics Equations

m_i	element mass per unit area
$\mathbf{u}_i$	element velocity
$\mathbf{r}$	element radius
f	Coriolis Parameter
ω_i	element angular velocity
$\check{\mathbf{f}}_{s,i}$	surface force
$\check{\mathbf{f}}_{b,i}$	body force
$\hat{\mathbf{F}}_{ij,n}$	contact force

Another notable difference from the AIDJEX era model dynamics is the lack of an internal force component that would lead to internal deformation in the particle. The continuum internal force components find analogous DEM forces in the form of the skin and body forces, where these forces are transmitted across a network of contacts rather than stress fields in the material. Development of any DEM must, because the elements have spatial scale and are forced by neighbor contact networks, handle the force network explicitly and with great care.

2.5 Discrete Element Simulator

To handle this critical task, this research and DEMSI will use Large-Scale Atomic/Molecular Massively Parallel Simulator (LAMMPS), a software suite developed by Sandia National Labs and available at http://lammps.sandia.gov, which is well suited for the scale of the model required for DEMSI and this research. LAMMPS is coded to handle granular interactions where the rigid particle approximation is more than sufficient. It explicitly computes the force networks for rigid elements in the simulation domain and integrates them through time. The software is efficient, having been optimized for massively parallel systems, open source and readily modifiable to customize to the needs of this research (Plimpton 1995). However, the rigidity assumption is insufficient for a basin scale model of sea ice as the elements increase in scale and internal deformation must be accounted for. At the

anticipated scaling of elements in DEMSI, 1 km diameter and 1 m thickness, the ice floe elements will not be able to be treated as rigid and techniques are required to explicitly describe element constitutive relationships and allow for permanent element deformation.

2.6 Thickness Distribution Generation

DEMSI's particle size limitation requires that a mechanism is in place to describe the resizing of elements as they deform. From their characteristic roughness for use in wind and current forcing, to thermodynamic and continuity requirements, the internal deformation of elements must be precisely calculated. A component of this development is the implementation of an analytic solution to sea ice ridging developed by Roberts and Coauthors (2019).

The solution argues that isostatic ridges, or those ridges that have reached maturity, can only exist along a single trajectory through the ridge strain, ϵ_R, potential energy density, $\mathcal{V}$, and macro-porosity, ϕ_R, state space. The solution developed in Roberts and Coauthors (2019) is enabled by the inclusion of Coulombic yield as the method of non-conservative energy dissipation. This inclusion constrains the solution space to a single trajectory dependent on the initial condition of the sea ice. From the solutions presented in Roberts and Coauthors (2019), the compressive strength of the pack can be estimated as well as any number of distribution dependent element properties critical to climate scale climate modeling. This work, however, has no data set with which to corroborate its findings. This thesis seeks to allay this deficit by generating a pressure ridge and plotting its ridge state evolution in the Roberts and Coauthors (2019) state space to assess the analytic solution.

THIS PAGE INTENTIONALLY LEFT BLANK

CHAPTER 3:
Model Description

The model of sea ice ridging that has been developed for this thesis uses LAMMPS to provide the underlying computational backbone and particle dynamics used. The model simulates sea ice as a three-dimensional granular material, where the individual grains are spherical particles. The pair-wise interactions are modeled using the Hertzian contact model (Silbert and Coauthors 2001).

This model seeks to recreate, in three dimensions, the two-dimensional pressure ridge model developed by Hopkins (1994). The Hopkins model simulates the generation of a pressure ridge by driving a virtual sheet of sea ice into a thicker, and stationary, ice mass. The moving sheet progresses through the initial buckling failure and generation of rubble to the piling of the rubble and creation of the ridge. By extending the Hopkins model to three-dimensions, additional degrees of freedom are gained enabling heterogeneity along the axis of the ridge to develop. This heterogeneity should provide greater insight into the distribution of ice thickness and mass along the ridge axis as well as the evolution of ridge state variables from initially undeformed ice to a mature ridge.

For this model, two sea ice plates are created by first populating two regions with spherical sea ice particles in a regular lattice structure. Next, the particles are bonded together if they are in contact to reinforce the lattice. Once the plates are created, an initialization integration is performed to bring the plates to hydrostatic balance at the virtual air-water interface at $z = 0$. With a system kinetic energy close to zero, a LAMMPS restart file is written to enable rapid re-initialization using different trial parameters. This restart file is then used to begin the trial in which one plate of sea ice is given an initial velocity with the forces of the extreme edge of the sheet set to zero. This zeroing of the force ensures that the extreme edge continues on at a constant velocity, driving the material of the sheet of ice into the second sheet to form the pressure ridge. For a schematic of this experiment setup refer to Figure 3.1.

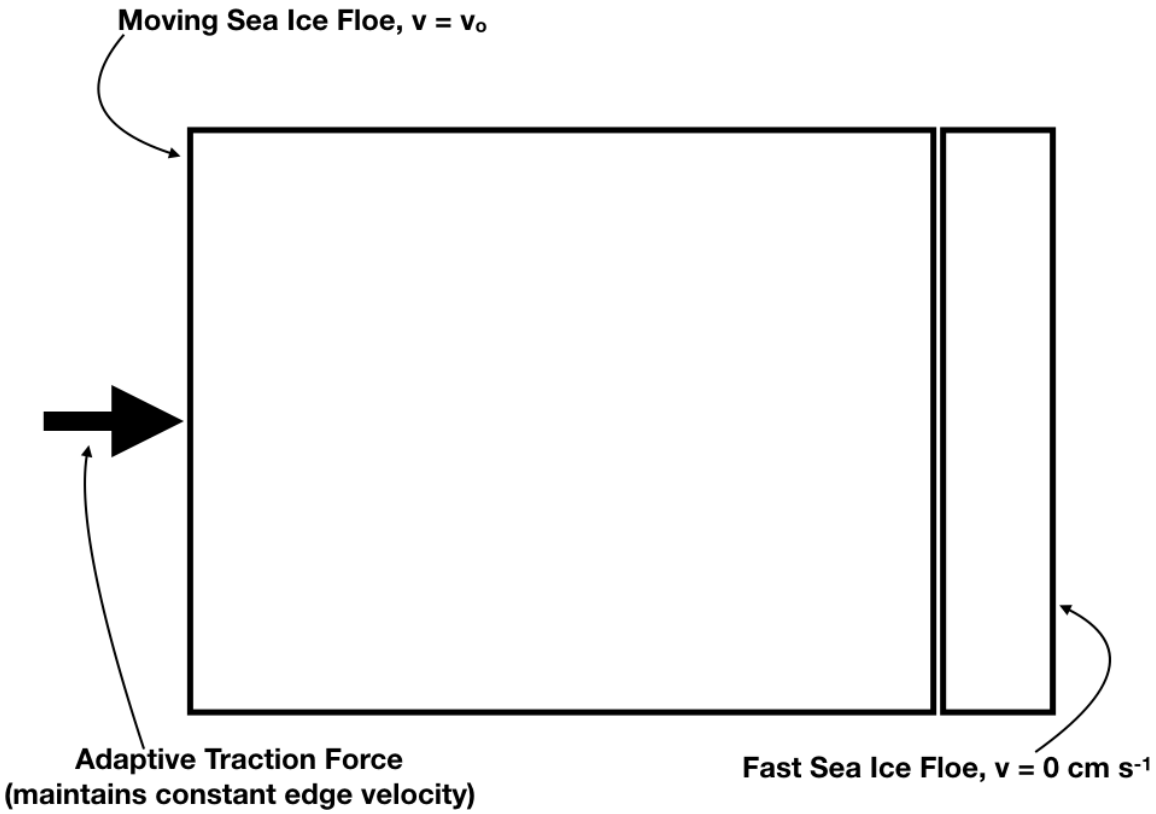

The simulation proceeds by driving two floes of sea ice together at constant velocity. The floe at left is given an initial velocity to the right. To maintain the convergence velocity, the forces at the extreme edge are set to zero. This ensures that the edge elements experience zero acceleration (and deceleration) ensuring that they have a constant velocity providing an adaptive traction force that ensure a constant convergence rate for the forming ridge.

Figure 3.1. Experiment Schematic

3.1 Particle Dynamics

There are three categories of forcing that each particle in the model is subject to: pair-wise interactions, bonded interactions, and body forces. The body forces provide the model gravity, buoyancy and particle drag, while the bond and pair-wise interactions define the rules by which the particles interact with one another as a simulation progresses.

3.1.1 Pair-wise Interactions

To simulate the interactions of unbonded particles with other particles, the model uses the LAMMPS Hertzian pair style. The pair-wise interaction describes the forces that particles exert on neighbors in contact. This intra-particle force, defined in Equation 3.1, includes contributions to the pair interaction from normal (first term) and tangential (second term) components.

$$F_{hz} = \sqrt{\delta}\sqrt{\frac{R_i R_j}{R_i + R_j}}[(k_n \delta \mathbf{n}_{ij} - m_{eff}\gamma_n \mathbf{v}_n) - (k_t \mathbf{\Delta s}_t + m_{eff}\gamma_t \mathbf{v}_t)] \tag{3.1}$$

LAMMPS (2017) defines Equation 3.1 and provides the definition of each term in the equation. Table 3.1, reproduced from LAMMPS (2017), summarizes the terms in Equation 3.1.

Table 3.1. Pair Style Definitions

δ	Overlap Distance of Particles i and j
k_n	Elastic Constant for Normal Contact
k_t	Elastic Constant for Tangential Contact
γ_n	Viscoelastic Damping Constant for Normal Contact
γ_t	Viscoelastic Damping Constant for Tangential Contact
m_{eff}	Effective mass of two particles of mass M_i and M_j
$\mathbf{\Delta s}_t$	Tangential Displacement Vector Between Two Particles
$\mathbf{n}_{ij}$	Unit Vector Along the Line Connecting Centers of Two Particles
$\mathbf{v}_n$	Normal Component of the Relative Velocity of Two Particles
$\mathbf{v}_t$	Tangential Component of the Relative Velocity of Two Particles

Reproduced from LAMMPS (2017).

The majority of these quantities are transparent to the user and are calculated without intervention. However, a number of the quantities are user defined in the input script for LAMMPS. The definition of the pair style requires the user definition of k_n, k_t, γ_n, γ_t, xmu, and a damping flag.

The elastic constants for contact, k_n and k_t, are defined for the Hertz case by Zhang and

Makse (2005) as

$$k_n = \frac{4G}{3(1-\nu)} \tag{3.2}$$

and,

$$k_t = \frac{4G}{2-\nu} \tag{3.3}$$

where, G and ν are the shear modulus and Poisson ratio, respectively. These definitions ensure the particles interact in a way consistent with real sea ice and are critical for the proper formation of the ridge from sea ice rubble.

The viscoelastic damping constants, γ_n and γ_t, are set to zero. A sensitivity analysis was performed on both parameters and neither appear to have any qualitative effect on the final ridge state. This finding is consistent with Silbert and Coauthors (2001). The final ridge configuration does show differences from simulations where these terms are included, but this is likely due only to the particle dynamics and has no bearing on the ridge state trajectory.

For granular materials, the slip condition is set using a Coulomb friction argument relating the maximum stable tangential force, F_t, to the normal force through

$$F_t = xmu\ F_n. \tag{3.4}$$

3.1.2 Bond Forces

Bonds in the simulation are used to ensure that the initial collection of sea ice particles maintain the initial lattice structure in their default undeformed state. The lattice structure chosen for this simulation, as depicted in Figure 3.2, is used to minimize bond orientation degrees of freedom and simplify bond parameterization.

To limit computational complexity, the model assumes that the bonds between particles are elastic, to a failure limit, and can be approximated by a simple spring such that,

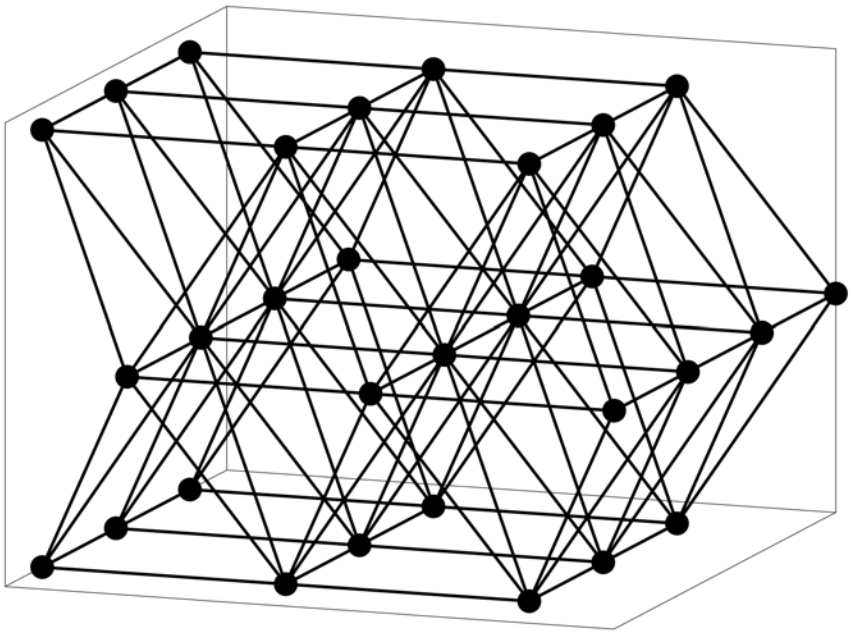

The basic configuration of bonds between elements at initialization. All bond lengths are $2 \cdot R_o$.

Figure 3.2. Floe Lattice Schematic

$$\mathcal{E}_{\text{bond}} = K_b \left(R_e - R\right)^2 \tag{3.5}$$

where, $\mathcal{E}_{\text{bond}}$ is the potential energy of the bond, K_b is the bond stiffness, R_e is the equilibrium bond length, and R is the instantaneous bond length. See Figure 3.3 for a schematic of an individual bond in its equilibrium configuration and a deformed state.

Determination of the appropriate bond stiffness was accomplished empirically through use of a virtual cantilever experiment in which a series of cantilever deflections were simulated. The results of each trial were then compared to an analytic Timoshenko cantilever solution which, given the same cantilever geometry, was adjusted by the elastic modulus to fit the analytic solution to the data. For details concerning this procedure, refer to Appendix A. The relationship of bond stiffness, K_b, to elastic modulus, E, is given by,

$$K_b = 0.06E. \tag{3.6}$$

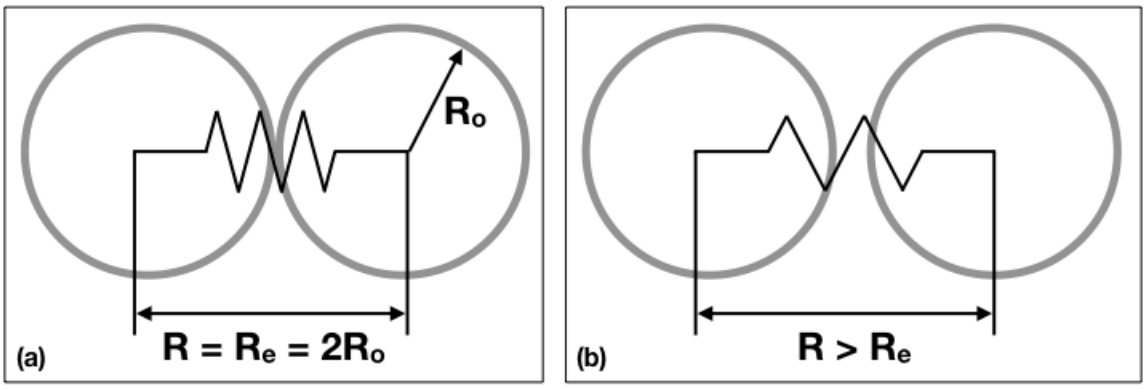

Illustrated are the (a) equilibrium and (b) deformed states of the bonds between particles in the simulation. R_e is chosen such that the undeformed, or $\mathcal{E}_{\text{bond}} = 0$, state of the lattice is close packed.

Figure 3.3. Bond Schematic

3.1.3 Bond Failure

To define the maximum extension of a bond, the tensile strength of sea ice is used to calculate the maximum bond deflection before failure. To derive a relationship between the tensile strength, $\sigma_{\max}$, and the maximum bond extension, $R_{\max}$, the force required to extend a region of ice by a distance Δx is first determined. The derivation begins with the definition of the elastic modulus,

$$E = \frac{\sigma}{\epsilon} \tag{3.7}$$

where σ and ϵ are the stress and strain, respectively, of the region of ice. By applying the definition of material strain, Equation 3.7 can be rewritten to find the maximum bond length, R_{max},

$$R_{\max} = R_e \left(1 + \frac{\sigma_{\max}}{E}\right). \tag{3.8}$$

3.1.4 Body Forces

To simulate the sea ice domain at the interface between the ocean and atmosphere, a series of field forces are also applied to each particle: gravity, buoyancy, and drag. All particles

are given an implicit downward gravitational acceleration of 9.8 m s^{-2} to approximate the effect of gravity at sea level.

To find the buoyancy force acting on each simulation particle, the volume of water it displaces is found as a function of the position of its centroid relative to the $z = 0$ plane. For the i^{th} element, the displaced volume is defined as

$$V_{\text{disp},i}\ (R_i, z_i) = \begin{cases} V_i & z_i \in (-\infty, -R_i] \\ V_i - \frac{\pi(R_i+z_i)^2}{3}(2R_i - z_i) & z_i \in (-R_i, 0] \\ \frac{\pi(R_i-z_i)^2}{3}(2R_i + z_i) & z_i \in (0, R_i] \\ 0 & z_i \in (R_i, \infty) \end{cases}$$

The buoyant force is therefore,

$$\mathbf{F}_{\text{buoyant}} = V_{\text{disp},i}\ \rho_{\text{sw}}\ \mathbf{g}. \tag{3.9}$$

Finally, each particle in the simulation is subjected to a damping force proportional to the particle's instantaneous velocity

$$\mathbf{F}_{\text{drag}} = \mu\ \mathbf{v}. \tag{3.10}$$

This force is included to augment simulation stability and return the particles to hydrostatic equilibrium as rapidly as possible. The damping constant is chosen such that a sphere of a given radius, R, is nearly critically damped. This value was chosen based on a series of numerical trials and is approximately 2 kg s^{-1} for particles with a radius of 0.1 m and mean density of 920 kg m^3.

3.2 Model Post-Processing

The raw model output produced by the simulation is dumped to an output at predetermined time intervals. This data is written such that the instantaneous position and particle variable states are correlated to each particle. For this study, the model outputs the position $(x, y, z)_i$,

R_i, ρ_i, $V_{\text{disp},i}$ and pressure. These properties only serve to provide the required input to compute the necessary ridge state variables: mean macro-porosity, mean potential energy density, and ridge-strain.

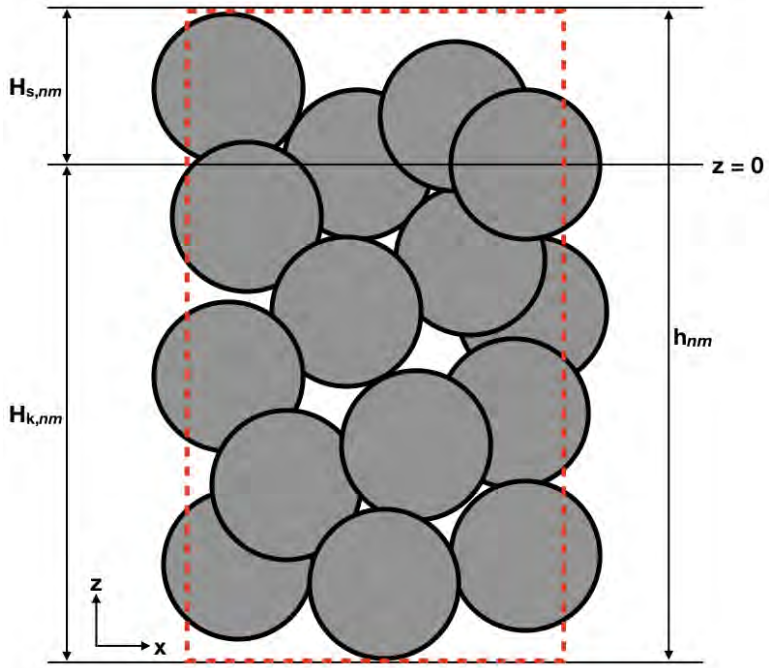

For sample interval (n,m), the measured free board, $H_{\text{s},nm}$, is given by the maximum positive vertical extent in the sample region. Similarly, the measured ice depth, $H_{\text{k},nm}$, is given by the maximum negative vertical extent. h_{nm} is the thickness of the sample region.

Figure 3.4. Vertical Sample Interval

Following from Roberts and Coauthors (2019), this work takes the LAMMPS output and performs procedures to compute the mean ridge state variables required to compute the simulated ridge state evolution for comparison with the analytic solution. Roberts and Coauthors (2019) computes the ridge state variables across the total extent of the ridge. Finding analogous ridge state values from this model though, requires that the grain-centric data output from LAMMPS be translated to find the same critical parameters used in the analytic solution. To do this, the simulation output must be mapped to an Eulerian grid on which further processing can be applied. However, because the model elements each have volume, the computation of the ridge variables $H(x, y, t)$, $\phi_R(x, y, t)$, and $\mathcal{V}(x, y, t)$ is complicated. The methods by which each of these variables are computed are outlined in

the following sub-sections.

3.2.1 Thickness, $h(x, y, t)$

The thickness of ice for a given sample area is the difference between the maximum and minimum vertical extents in the area. For an illustration of this in principle, see Figure 3.4. This defines the local ice thickness for the sample area, h_{nm}. This is done to approximate the convex hull containing each of the simulated particles. Keeping the sample region relatively small in relation to the size of the particles ensures that the error introduced to the sample area's thickness, h, is small.

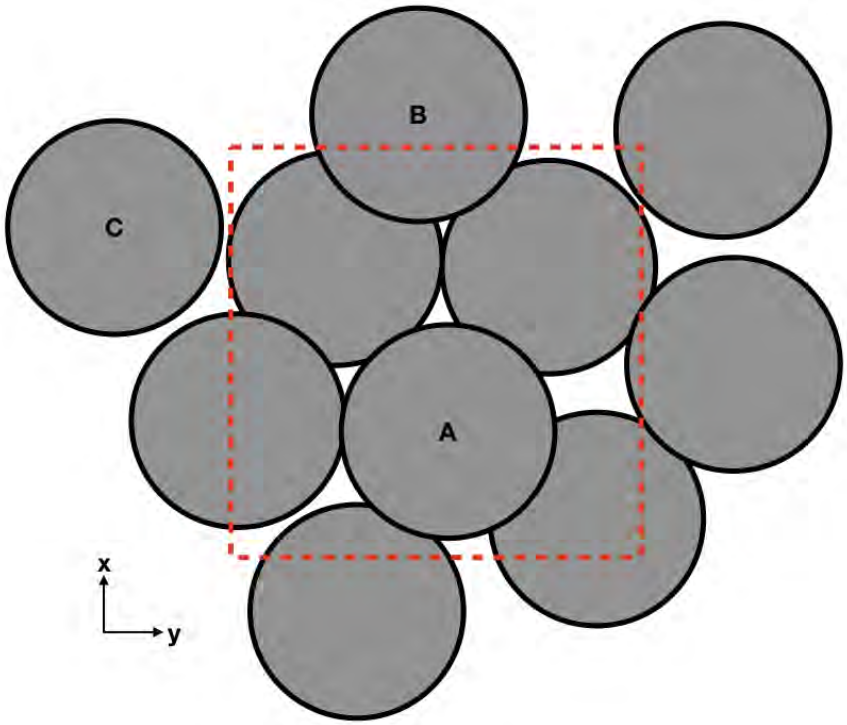

For sample interval (n,m), particle A is fully contained within the sample region and has a VWF of 1. Particle B is partially in the region and has a VWF between 0 and 1. Finally, Particle C has no portion within the sample region and has a VWF of 0.

Figure 3.5. Horizontal Sample Interval

3.2.2 Macro-Porosity, $\phi_R(x, y, t)$

Macro-Porosity is the volume of void space in a sample volume. It is defined as, $\phi_R = 0$ for undeformed ice and $\phi_R = 1$ for a region that is devoid of sea ice. The computation of ϕ_R from data first requires the calculation of the void fraction in the sample area,

$$\phi = 1 - \frac{V_{\text{ice}}}{V_{\text{ridge}}}. \tag{3.11}$$

The volume of the ridge in the sample area is simply,

$$V_{\text{ridge},nm} = \left(H_{\text{s},nm} - H_{\text{k},nm}\right) x_s y_s = h_{nm} x_s y_s \tag{3.12}$$

where, x_s and y_s are the dimensions of the grid size in the x and y directions, respectively.

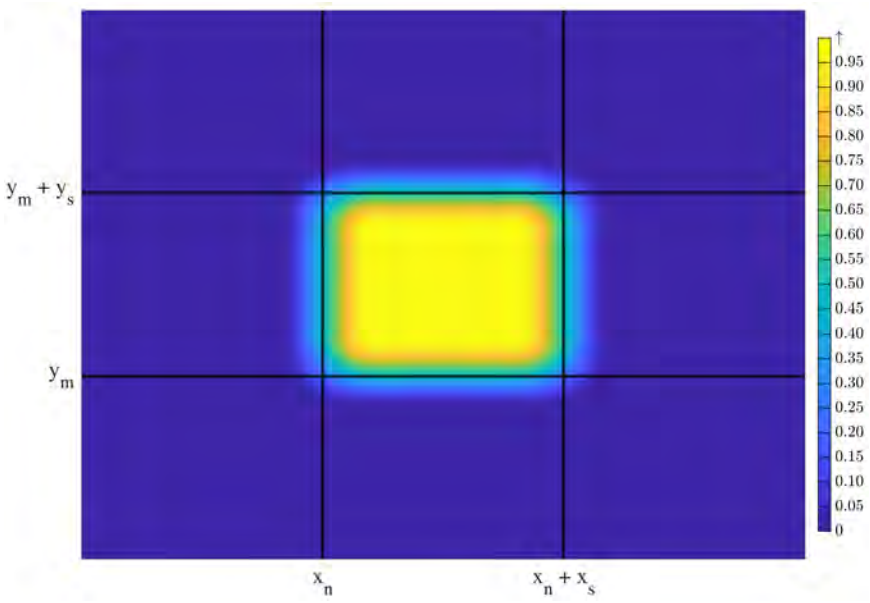

Evaluated for a sample region size of 0.5 m x 0.5 m and particle radius of 0.1 m. The heat map for Volume Weighting Function enables the computation of ϕ and $\mathcal{V}_R$ within a sample region accounting for sample grid overlap.

Figure 3.6. Volume Weighting Function

As shown in Figure 3.5, particles in the sample area do not necessarily contribute their full volume to the region. Particles near the sample area boundary partially contribute their

volume to the sample area and neighboring areas. To account for this boundary overlap, a VWF is derived. The VWF serves as a multiplication factor to properly distribute a particle's volume. The VWF is computed as a function of of x_s, y_s, and R_o. The volume contained within the sample area is calculated for a particle of given radius. This is computed for all x and y on which a particle could contribute a portion of its volume to the sample area to produce a heat map. An example of the output is shown in Figure 3.6. Therefore, V_{ice} is defined as,

$$V_{\text{ice}} = \sum_{i=1}^{N} V_i \, VWF \tag{3.13}$$

where, N is the list of particles that could contribute to the volume of ice within the sample region.

Bulk porosity, ϕ, of the region normally has two contributions: micro-porosity, ϕ_{micro}, or the porosity associated with ice crystal inclusions like brine pockets, and macro-porosity, ϕ_R, or the porosity associated with the generation of rubble in the deformation of the ice floe. For the simulated sea ice floe, the bulk porosity is defined as,

$$\phi = \phi_R + \phi_{\text{micro}}. \tag{3.14}$$

Micro-Porosity, ϕ_{micro}, is an artifact of the formation of the initial ice floe and is a property of sea ice. For purposes of this study, its contribution only manifests in the mechanical properties of sea ice, and is assumed to be zero for these calculations. Therefore, Equation 3.14 reduces to,

$$\phi = \phi_R. \tag{3.15}$$

However, it is clear that by simulating sea-ice as a granular solid comprised of a number of spherical grains, a third, artificial, void source is introduced. The space between particles in the undeformed lattice represents a lower limit to which the macro-porosity can be calculated. To correct for this source of additional void, the computed porosity values are

interpolated to have a range between 0 and 1.

$$\phi_R = \frac{\phi - \bar{\phi}_o}{1 - \bar{\phi}_o} \tag{3.16}$$

where, $\bar{\phi}_o$ is the bulk porosity of the undeformed source ice and is the lower limit of ϕ_R for the simulation.

3.2.3 Potential Energy Density, $\mathcal{V}(x, y, t)$

The total potential energy of a sample area proceeds along similar lines as the calculation of the total volume of ice in the sample area. A particle near the sample boundary will only contribute a portion of its total potential energy to the sample area and must be modified by the VWF. Therefore, the potential energy density is defined as,

$$\mathcal{V} = \frac{\sum_{i=1}^{N} PE_i \; VWF}{x_s \; y_s}. \tag{3.17}$$

To calculate the potential energy of a particle in the simulation, PE_i, the work done to displace a particle from $z = 0$ to $z = z_i$, is first calculated.

$$W_i = -\int_0^{z_i} F_{z,i} dz \tag{3.18}$$

where, $F_{z,i}$ is the vertical component of the field forces acting on the i^{th} particle, specifically gravity and buoyancy. Additionally, as a particle is submerged, it displaces some amount of water vertically. The displaced sea water is assumed to lift exclusively in the sample region and is spread evenly. This displaced water's potential energy is computed at its center of mass. Therefore, the total potential energy of a particle is given by

$$PE_i = W_i + m_{\text{disp},i} \; g \; h_{\text{disp},i} = W_i + \left(V_{\text{disp},i} \; \rho_{\text{sw}}\right) g \left(\frac{1}{2} \frac{V_{\text{disp},i}}{x_s \; y_s}\right). \tag{3.19}$$

3.3 Ridge State Evaluation

The ridge state is a three-dimensional relationship between the ridge strain, ϵ_R, the mean macro-porosity, $\bar{\phi}_R$, and the mean potential energy density, $\bar{\mathcal{V}}$. In Roberts and Coauthors (2019), coarse graining was used for mathematical expediency, but here, it is used here to identify the ridging region and consistency with that study. Ultimately the coarse-grain profiles are not used in any calculations for the ridge state. However, the coarse-grained profile is less sensitive to local variability within the ridge profile. This leads to enhanced ridge domain certainty and is effective in rejecting portions of the simulation domain that do not contribute to the primary ridge.

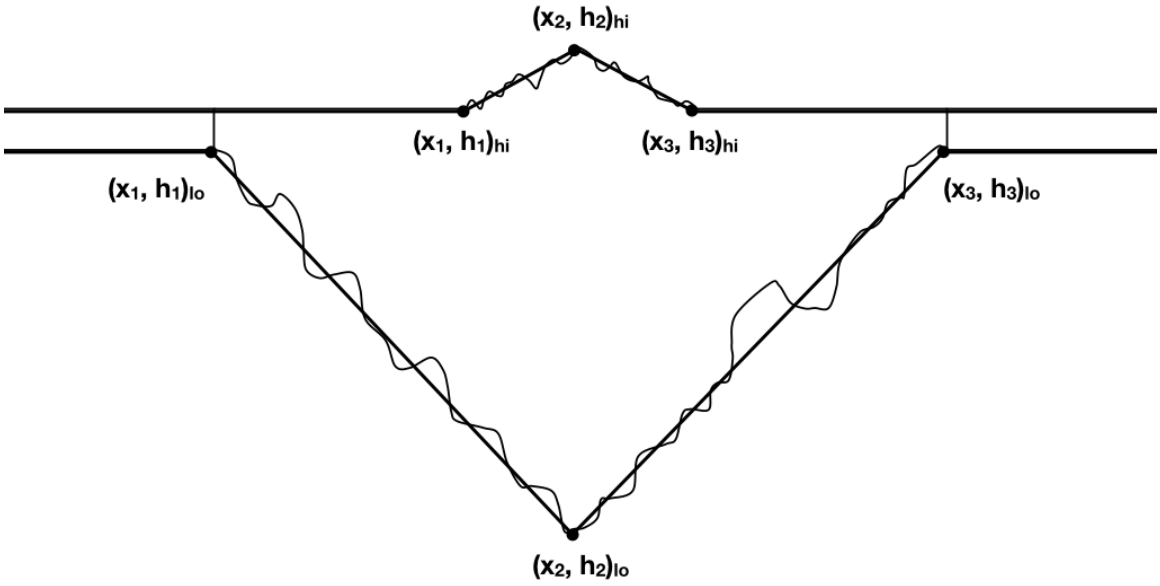

The coarse-grained ridge shape is determined by curve fit on the mean ridge profile as a function of time. This coarse-grained region defines the limits over which the ridge state variables are evaluated.

Figure 3.7. Pressure Ridge Coarse Grain Schematic

Finding the coarse-grained profile is done by applying a curve fit algorithm to the mean sail, H_s, and mean keel, H_k, profiles. This process identifies the ridge domain for evaluation of ridge strain, ϵ_R, mean macro-porosity, $\bar{\phi}_R$, and mean potential energy density, $\bar{\mathcal{V}}$, for the ridge. The coarse-grained profiles, illustrated in Figure 3.7, are both piece-wise functions defined as,

$$H_c(x,t) = \begin{cases} h_1 & x \in (-\infty, x_1] \\ h_1 + \frac{h_2 - h_1}{x_2 - x_1}(x - x_1) & x \in (x_1, x_2] \\ h_2 + \frac{h_3 - h_2}{x_3 - x_2}(x - x_2) & x \in (x_2, x_3] \\ h_3 & x \in (x_3, \infty) \end{cases}$$

.

The ridge domain is defined for the lower limit as the minimum of $x_{1,\text{lo}}$ and $x_{1,\text{hi}}$ and for the upper limit as the maximum of $x_{3,\text{lo}}$ and $x_{3,\text{hi}}$. Ridge parallel transect means of macro porosity and potential energy density profiles are also found and are defined as,

$$\phi_{R,\text{trans}}(x,t) = \frac{1}{y_{\max} - y_{\min}} \int_{y_{\min}}^{y_{\max}} \phi_R dy \tag{3.20}$$

and

$$\mathcal{V}_{\text{trans}}(x,t) = \frac{1}{y_{\max} - y_{\min}} \int_{y_{\min}}^{y_{\max}} \mathcal{V} dy. \tag{3.21}$$

The state of the simulated ridge is evaluated by first computing the ridge strain, derived by Roberts and Coauthors (2019),

$$\epsilon_R(t) = \frac{H_F - H_R}{H_R} \tag{3.22}$$

where, H_F is the thickness of the un-deformed ridging ice and H_R is the imporous thickness of the ridged ice. For this work, it is defined as

$$H_R(t) = \frac{1}{W_{\text{ridge}}} \int_{\text{ridge}} (H_s - H_k)\,(1 - \phi_{R,\text{trans}}) dx \tag{3.23}$$

where, W_{ridge} is the width of the ridge domain. Finally, $\bar{\phi}_R$ and $\bar{\mathcal{V}}$ are computed. Each are mean sea ice thickness weighted averages of the transect profiles and are defined as,

$$\bar{\phi}_R(t) = \frac{\int_{\text{ridge}} (H_s - H_k)\, \phi_{R,\text{trans}} dx}{\int_{\text{ridge}} (H_s - H_k)\, dx} \tag{3.24}$$

and,

$$\bar{\mathcal{V}}(t) = \frac{\int_{\text{ridge}} (H_s - H_k)\, \mathcal{V}_{\text{trans}} dx}{\int_{\text{ridge}} (H_s - H_k)\, dx}. \tag{3.25}$$

THIS PAGE INTENTIONALLY LEFT BLANK

CHAPTER 4:
Simulation Results

To generate a pressure ridge and evaluate its trajectory through ridge state space, an integration was completed where a 0.4 m thick sheet of ice collides with a 1 m thick sheet at 0.02 m s^{-1}. The model was then integrated for 10 minutes of simulated time. Details of the trial and values of the important parameters are detailed in Table 4.1. The simulation appears to produce a reasonable facsimile of a pressure ridge, demonstrating the characteristic shape with a large keel and small sail, orientation normal to the direction of convergence and irregular packing that indicates the development of macro-porosity. An interesting result of this research that was not pursued, but briefly outlined in Appendix B, is the apparent ability of the model to generate acoustic waves in the simulated material.

Table 4.1. Simulation Configuration

Floe 1	100 x 50 x 0.4 m	Floe 2	5 x 50 x 1 m
ρ_{ice}	920 kg m^{-3}	ρ_{sw}	1020 kg m^{-3}
μ	2 N s m^{-1}	E	0.67 - 1.0 GPa
ν	0.3	σ_{max}	350 - 750 kPa
v_o	2 cm s^{-1}	T	600 s
dt	50 μs	R_o	0.10 m
x_s	0.5 m	y_s	0.5 m

4.1 Pressure Ridge Generation

The model is able to produce pressure ridges that are consistent with the general ridge profile outlined in Figure 2.1. The shape is characterized by the large, pronounced keel and smaller sail, which are clearly evident in Figure 4.1. Additionally, the ridge has heterogeneity in aspect along the ridge axis, indicating that this modeling scheme produces a more reasonable simulated ridge state where more natural ridging processes are allowed to progress. From a view above the simulation, Figure 4.2 shows more clearly the final primary ridge extent. Additionally, evident is a small secondary ridge near the center of the simulation domain. This ridge is not included in computations of the ridge state evolution, but is important

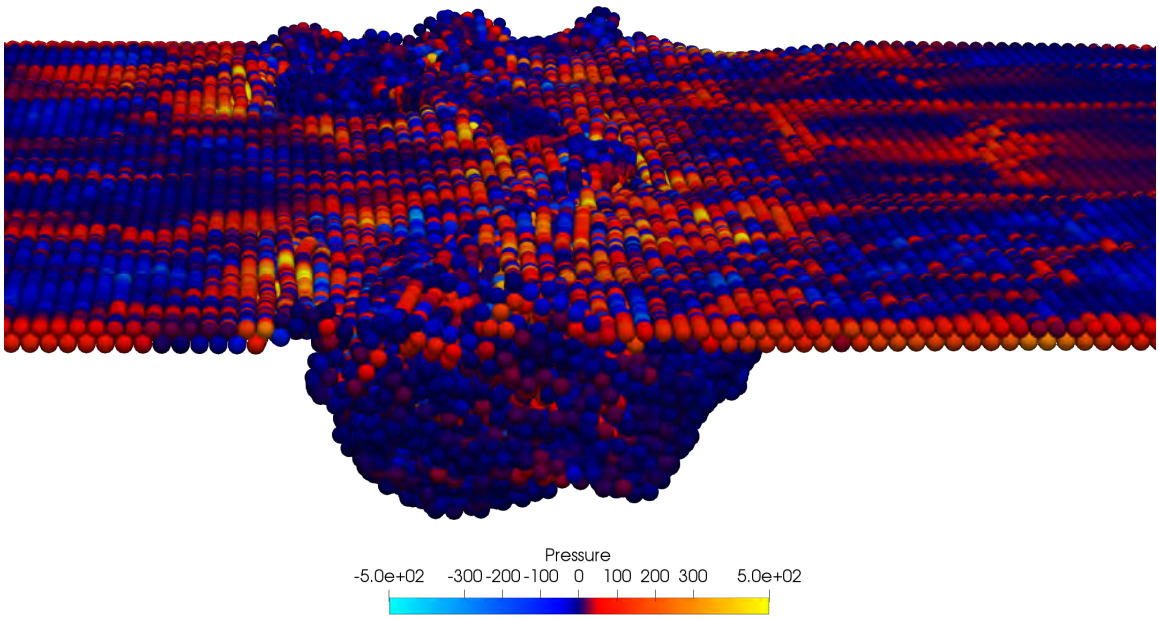

Pictured is the final simulation result in profile. The pronounced ridge is apparent at the center of the frame. The ridge has the characteristic sail and keel shape. The simulation was integrated for 10 minutes simulated time and has 294,325 granular elements. A video of this evolution for the duration of the integration is available at Davis (2019b).

Figure 4.1. Final Ridge, Profile View

because it shows a non-local fracture pattern and the ability of the model to create local deformations that are semi-independent of other failure regions.

Interestingly, the field also shows two ways in which stress is transmitted through the material. At the failure interface where piled rubble is the primary constituent, the stresses are transmitted through highly localized stress singularities that effectively cause continuous cracking and rubble generation. However, isolated from these rubble zones, the stress field is diffuse, even in regions where the lattice structure is highly disrupted. This diffuse stress indicates that even though the particles are no longer bonded, they are still behaving as a cohesive, continuous material.

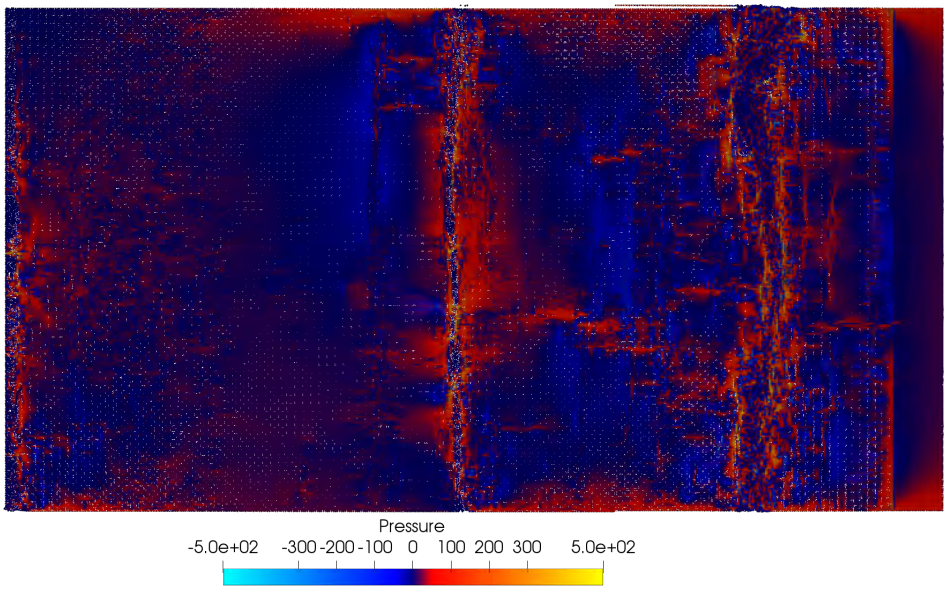

Pictured is the final simulation result from above. The primary ridge near the right of the plate with a pressure network emanating from the rubble region is apparent. Near the center of the plate is a secondary ridge forming after the primary fracture at the start of the simulation. A video of this evolution for the duration of the integration is available at Davis (2019a).

Figure 4.2. Final Ridge, Plan View

4.2 Simulation Remapping

With a reasonable ridge's evolution through time available, the time dependent ridge state evolution can be computed. This computation starts with the remapping procedure, outlined in Section 3.2, to calculate the ridge state variables as a function of a regular grid. The grid spacing chosen is 0.5 m. Results of this remapping process are presented in Figures 4.3, 4.5, and 4.4 where the ice thickness ($h(x, y, t)$), macro-porosity ($\phi_R(x, y, t)$), and potential energy density ($\mathcal{V}(x, y, t)$), respectively, are shown.

Figure 4.3 shows well the initial formation of the ridge where the initial, relatively wide fracture region is consolidated into a pressure ridge. As the ridge continues to grow, more rubble is added, the thickness increases, and the ridge widens until it reaches maturity by the end of the simulation. The thickness along the ridge axis is also highly variable showing the

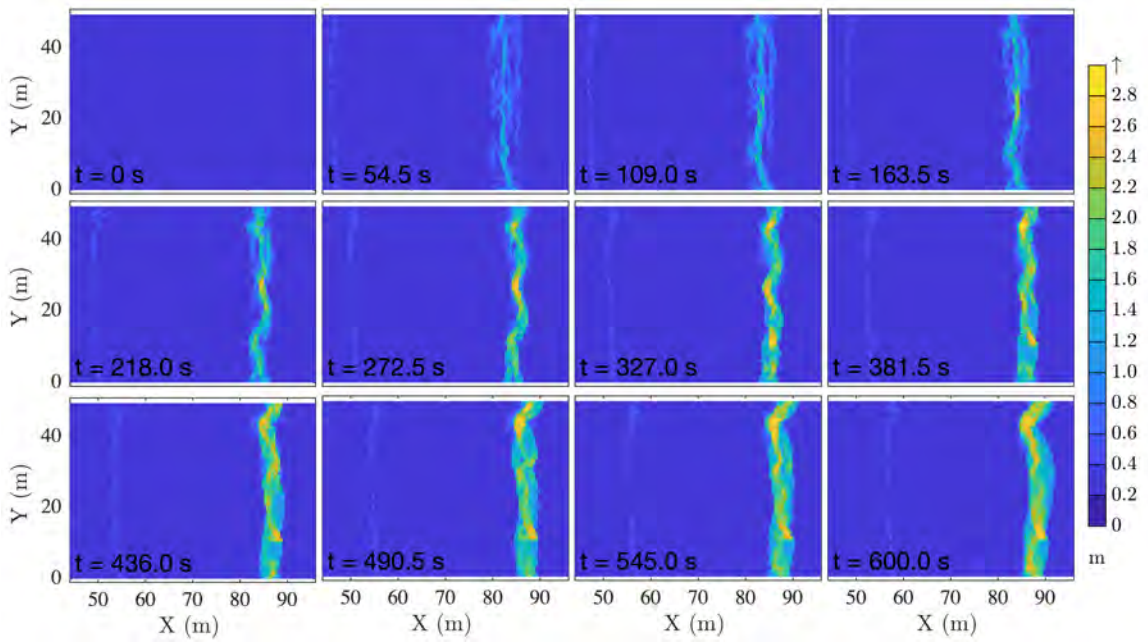

The ridge thickness, h, evolves from the initial fracture field evident at t = 54.5 s. The primary ridge axis first consolidates then both widens and becomes more pronounced as the ridge matures. Strong heterogeneity is evident in each ridge state indicating the model's ability to generate ridge states that capture variability in all three dimensions.

Figure 4.3. Thickness Plan View Evolution

presence of local ridge thickness maxima that move along the ridge axis as the additional degree of motion enables mass redistribution along the ridge axis.

Figure 4.4 shows the evolution of $\mathcal{V}$ as the simulations proceeds. As the ridge forms, particles are driven from the water interface and are given potential energy. The total potential energy in the field clearly increases in the ridging region and is relatively unchanged in the non-ridging regions. The regions of relatively high $\mathcal{V}$ near the simulation boundaries to the left and right indicate, at right, the thick, fast ice and some local deformation at the moving edge due to the necessary stress discontinuity required to drive the sheets together. Note that there is a secondary ridge axis that develops near the center of the domain in this particular simulation. This secondary ridge never reaches sufficient maturity, or size, to be identified by the techniques outlined in Section 3.2 and is therefore not included in the following ridge state calculations.

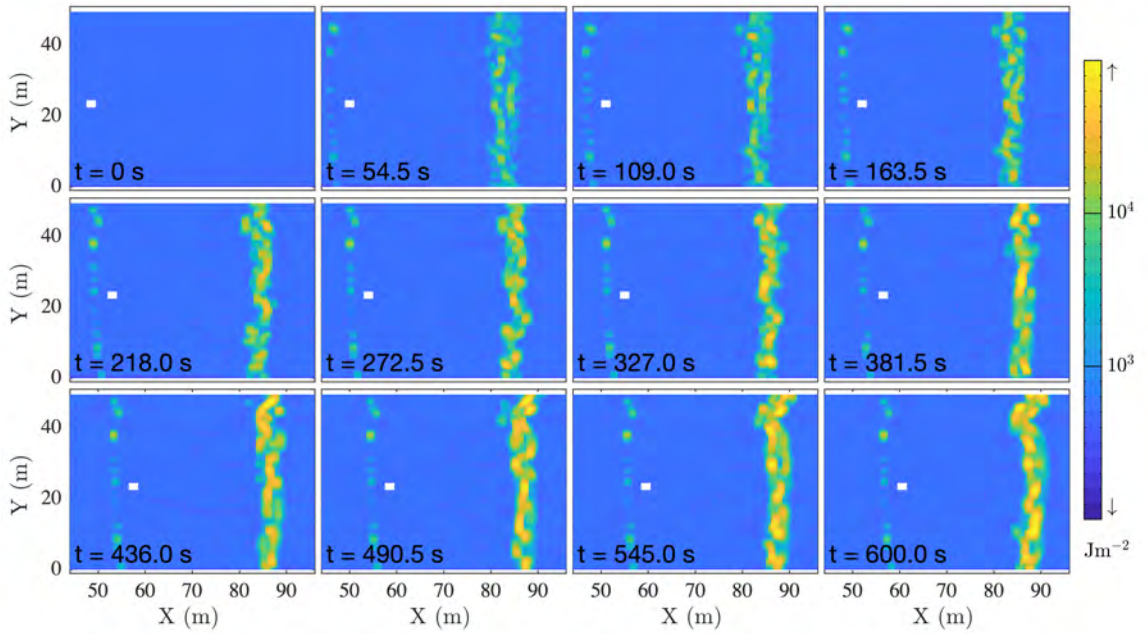

The potential energy density, $\mathcal{V}_R$, evolves over the course of the simulation. A secondary ridge axis is also apparent that forms during the initial fracture event and advects across the simulation. The frame at $t = 0$ s shows some minor numerical artifacts introduced due to a type of aliasing between the post processing scheme and the regular lattice.

Figure 4.4. Potential Energy Density Plan View Evolution

Finally, Figure 4.5 demonstrates the evolution of ϕ_R. Of particular note is the convergence of the initial fracture zone where the initial source of rubble is created. Once this region is compacted, normal ridge growth resumes and the ridge widens. The secondary ridge axis near the center of the field is also evident. These fields are of particular use in identifying failure regions that are not visible in figures 4.3 and 4.4.

4.3 Ridge State Evaluation

To determine the ridge state trajectory, first the mean ridge profile is evaluated. Figure 4.6 shows the development of the ridge profile through the simulation duration. Apparent at t = 54.5 s to t = 109.0 s are the artifacts of the initial fracture of the floe. These buckles show the divergence of the pack from a typical pressure ridge profile and do not present the normal keel and sail structure. However, as the simulation carries on, the rubble region is consolidated and a typical ridge profile emerges by t = 163.5 s. It is on this profile that the

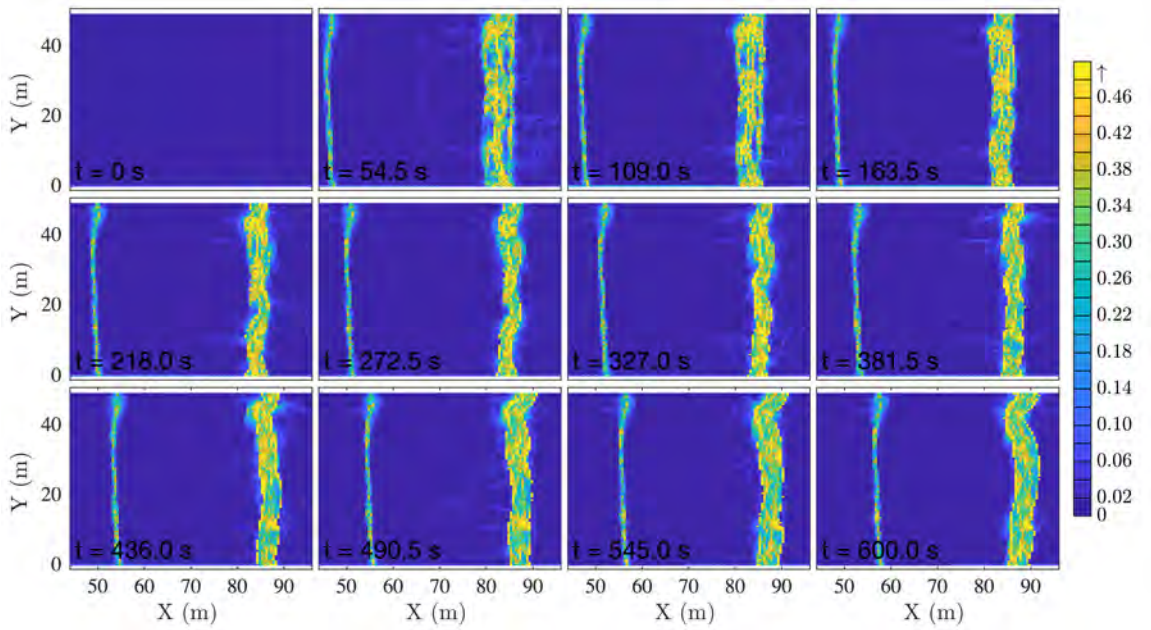

Macro porosity field as a function of simulation time. The initial fracture event is evident in the large introduction of macro porosity at the ridge axis. The porous region, right after fracture, is wide and somewhat diffuse. However, like Figure 4.3, the macro-porosity is quickly consolidated and shows the same development as the thickness field.

Figure 4.5. Macro Porosity Plan View Evolution

ridge coarse-grain profile is fit to ascertain the horizontal, along the x direction, domain of the ridge. At every time step, the coarse-grain profile is fit to the mean ridge profile. Each ridge state variable is then computed over the determined ridge domain.

Figure 4.7 shows the development in time of each of the ridge state variables. All three variables show a large discontinuity at approximately t = 50 s that coincides with the large catastrophic failure of the ridging region. At this instant, the ice buckles generating a large field of rubble on which the new ridge will begin its formation. Furthermore, this instantaneous rubble generation is also evident in the macro-porosity signal where the majority of the porosity is generated during the fracture event with relatively minor contributions occurring thereafter.

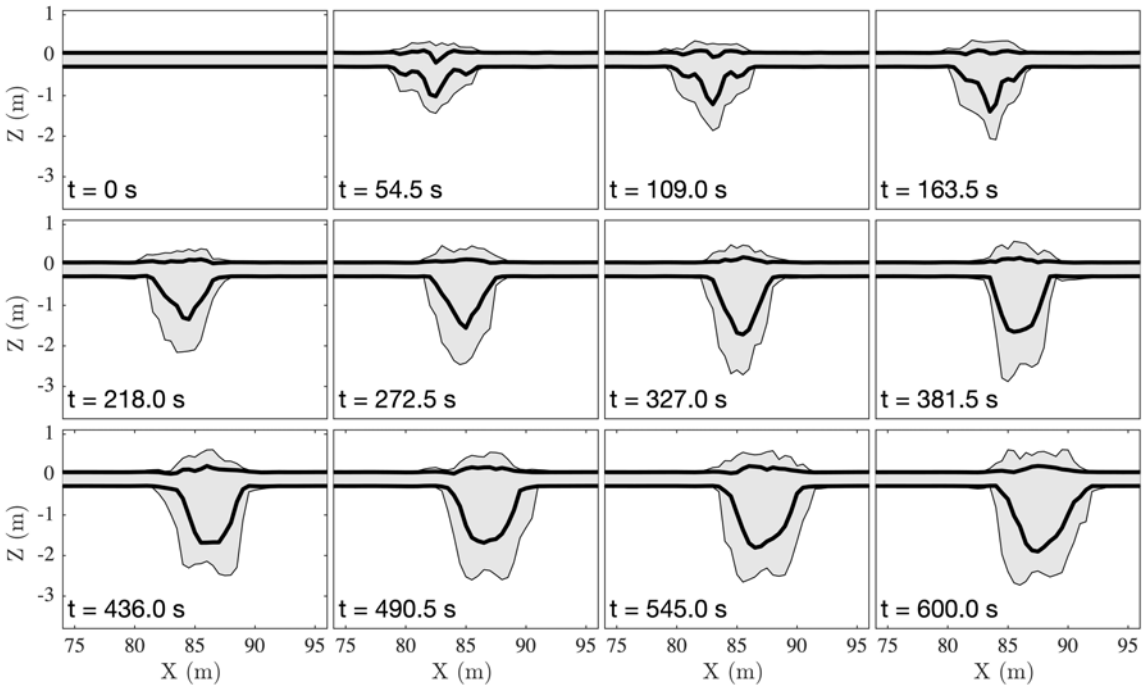

The mean ridge is indicated by the bold line. The shaded region shows the maximum three-dimensional ridge extent in the data. The ridge appears to reach a quasi-static state in the last quarter of the simulation where the ridge does not appear to grow and only moves across the simulation domain.

Figure 4.6. Mean Ridge Profile Evolution

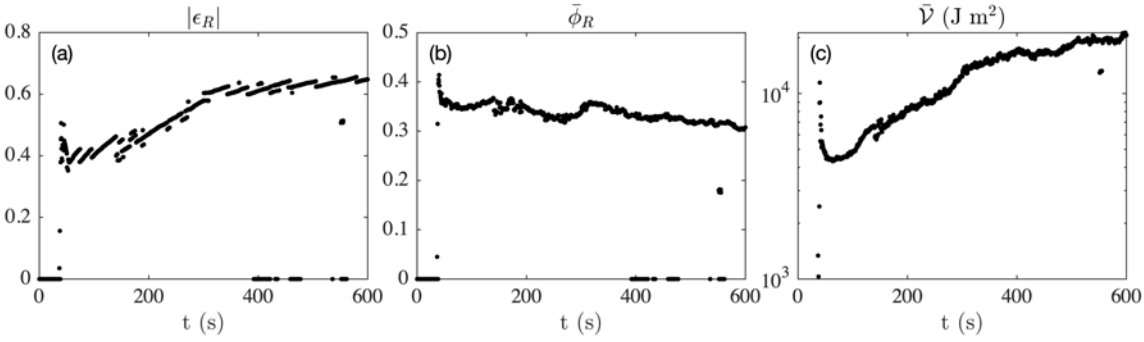

The ridge state variables of ϵ_R, $\bar{\phi}_R$, and $\bar{\mathcal{V}}$ are plotted in (a), (b), and (c), respectively. The initial failure early in the simulation shows the rupture of the moving ice sheet. All three variables begin to show asymptotic behavior late in the simulation.

Figure 4.7. Ridge State Variables Evolution

THIS PAGE INTENTIONALLY LEFT BLANK

CHAPTER 5:
Discussion and Conclusions

The model developed in this thesis largely corroborates the analytic solution developed by Roberts and Coauthors (2019) to the ridge state trajectory and demonstrates the ability to simulate high resolution ridge formation in a virtual state. This development enables further investigation of the mechanical response of undeformed sea ice to forcing and is valuable in investigations requiring greater temporal granularity and scaling than is available from ridge observations.

5.1 Comparison to Variational Ridging Solution

This model and the analytic solutions derived by Roberts and Coauthors (2019) both seek to bridge the gap in sea ice observations for the distribution of ridge states in the pack. The model creates a virtual ridge and calculates the evolution of its ridge state. This is done to determine how the ridge state changes in time as well as its final isostatic configuration to understand the redistribution of mass, under strain, of a single pressure ridge. It makes a number of critical assumptions, chief among them is that sea ice can be modeled as a granular material with simple elastic bonds binding the grains together into a floe, that lead to the emergence of an isostatic ridge with a simple convergence scheme. However, it only creates a single ridge. Natural sea ice under convergence generates many small ridges distributed through the pack. Potentially, with sufficient scaling, this model could generate a more representative distribution of ridges if the simulation domain is sufficiently increased. This ability is hinted at with the apparent emergence of a secondary ridge axis in the simulation, as shown in Figure 4.2.

Whereas the model uses element bonding and a Hertzian contact parameterization to give the material the ability to bear internal stress states and develop into a ridged configuration, the Roberts and Coauthors (2019) solutions use a Coulombic friction model to determine a critical angle of repose and a coarse-grained profile to determine the isostatic shape of a ridge. The Coulombic friction assumption constrains the solution space to a single trajectory enabling expedient solving for use in ESMs, but potentially does not capture the totality of valid isostatic ridge configurations (Roberts and Coauthors 2019).

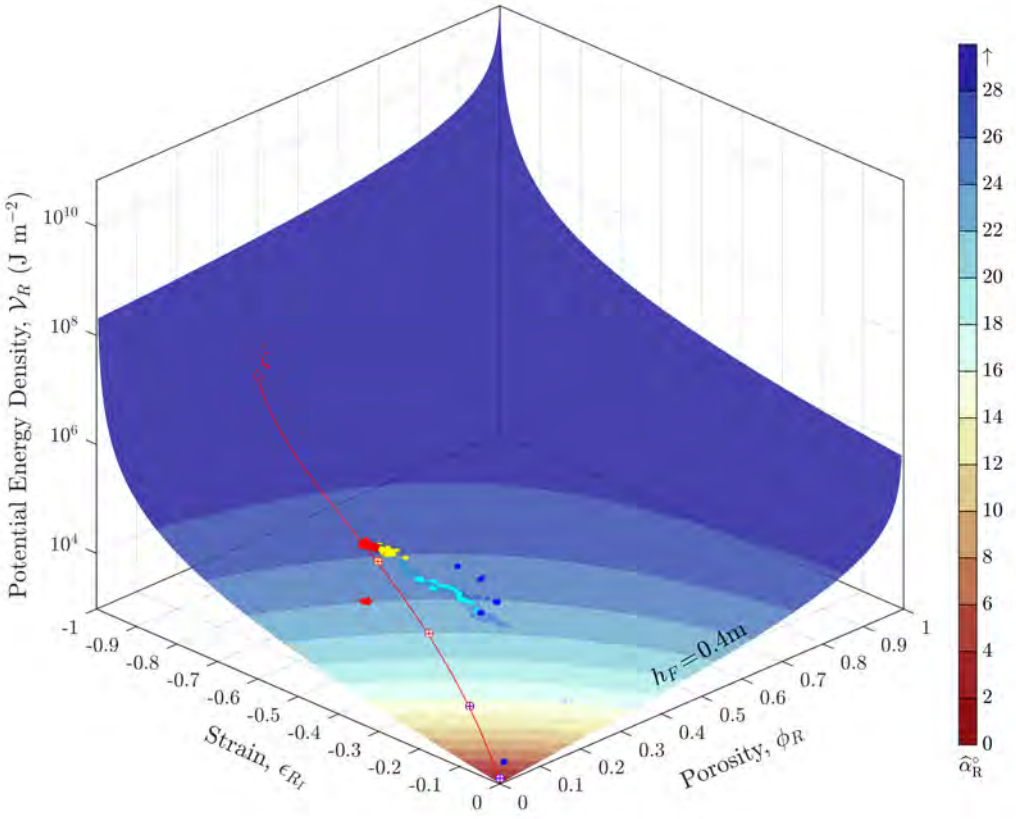

The analytic solution to the ridge state manifold for feed ice of $h_F = 0.4$ m with simulated ridge state evolution points. The red trajectory curve is the analytic solution that satisfies the undeformed sea ice initial condition. The simulated ridge state values diverge from the analytic trajectory at low strains, but converge at moderate ridge strain values as the ridge matures. The simulated ridge state evolution is colored by quarter of simulated time; 0-150 s in blue, 150-300 s in cyan, 300-450 s in yellow and 450-600 s in red.

Figure 5.1. Ridge State Manifold. Adapted from Roberts and Coauthors (2019).

Though the two ridging techniques presented are different, the ridge state evolution of the model converges with the analytic ridge state trajectory when the simulated ridge reaches maturity. The convergence of the two approaches is evident in Figure 5.1. The immature ridge, colored in blue and cyan, is a relatively diffuse rubble field that has not yet gone through a consolidation process caused by continued convergence of the floes. As the ridge reaches maturity, colored in yellow and red, the evolution of the ridge converges

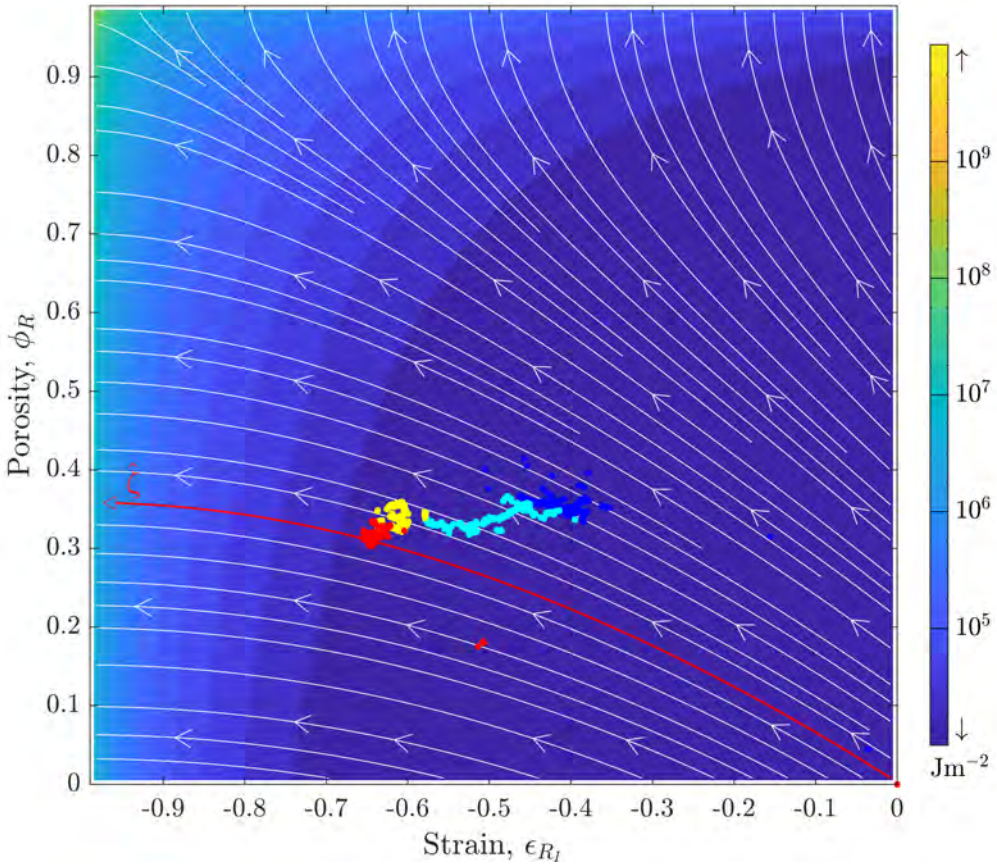

The ridge state manifold is projected onto (ϵ_R,$\bar{\phi}_R$) space. The white lines are the dilation field and possible ridge state trajectory solutions for different initial conditions. The analytic solution (red line) satisfies the initial condition of undeformed ice. The modeled ridge states are plotted and show the convergence of the simulation to the analytic solution at moderate strain levels. The simulated ridge state evolution is colored by quarter of simulated time; 0-150 s in blue, 150-300 s in cyan, 300-450 s in yellow and 450-600 s in red.

Figure 5.2. Ridge State Projection. Adapted from Roberts and Coauthors (2019).

with the theory and stops evolving with only minor fluctuations due to continued fracture and rearrangment of the simulated elements. At low to moderate strains, the lack of consolidation manifests as enhanced ϕ_R relative to the theoretical isostatic ridge state for the same ϵ_R. This result is potentially consistent with the theory because the rubble field is still undergoing rapid transition and cannot be considered isostatic. However, it could also

be the result of the large difference in element sizing in this model versus the assumption of very small rubble elements in the theory. Further work is required to determine if the model, with smaller element sizing and very slow convergence, could track more closely with the ridge state trajectory by allowing each point in the simulated ridge evolution to be quasi-isostatic.

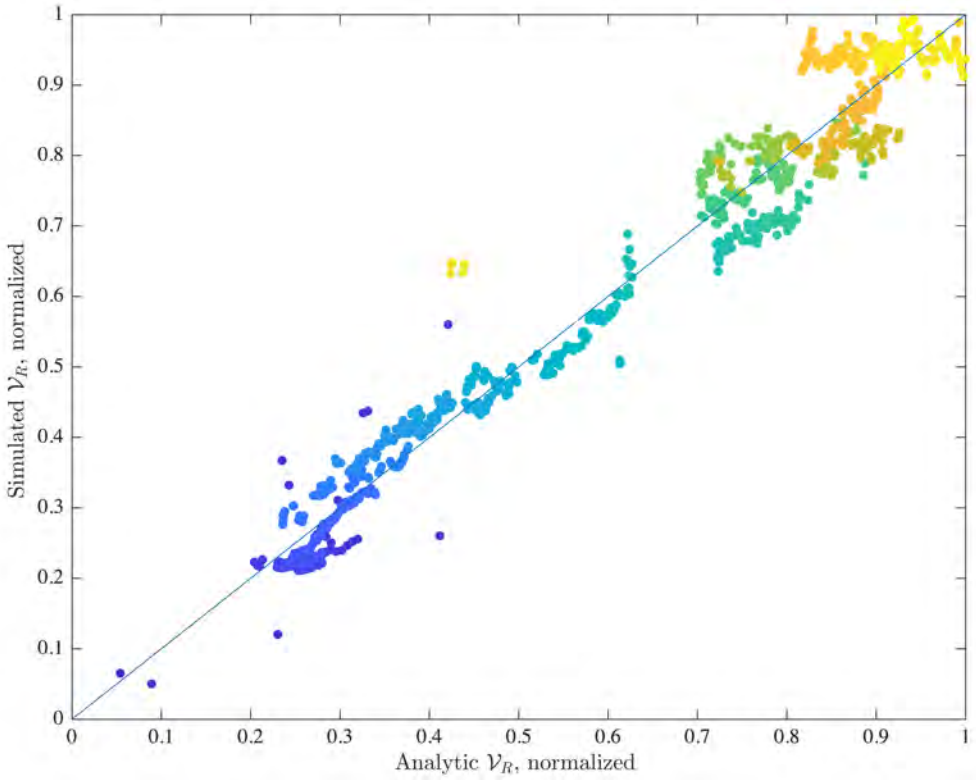

Normalized $\mathcal{V}_R$ for both the analytic ridge state trajectory solution derived by Roberts and Coauthors (2019) and the simulated ridge state evolution. The points are colored by simulation time; blue is early in the simulation evolving to yellow. The data shows close agreement (Pearson Correlation Coefficient of 0.988) at all states. By the end of the simulation the ridge state evolution converges strongly with the analytic solution and represents a quasi-isostatic mature ridge consistent with theory. Outliers are caused by instances of mean profile coarse-graining failures.

Figure 5.3. Normalized Numerical and Analytic $\mathcal{V}_R$ Comparison

The convergence of the three ridge state variables (ϵ_R, $\bar{\phi}_R$, and $\bar{\mathcal{V}}_R$) is more clearly illustrated in Figures 5.2 and 5.3. Figure 5.2 shows well the convergence of ϵ_R and ϕ_R. With the same coloration of the simulated ridge state evolution as in Figure 5.1, the convergence of the

two solutions, once the simulated ridge reaches maturity, is illustrated. The coarse-graining method employed in this thesis to identify the ridging region's domain in the simulation misses much of the evolution just after the initial fracture event because the rubble field has not yet consolidated to a point where it has the characteristic ridge shape. However, the data available at instances early in the simulation hint at ridge states that are undergoing rapid transition with high ϕ_R for the current ϵ_R. Interestingly though, Figure 5.3 demonstrates that at all instances in the evolution of the simulated pressure ridge, the $\mathcal{V}_R$ of the analytic ridge state trajectory and the simulated ridge evolution are in close agreement. This indicates that while the arrangement of the grains in the simulation is inconsistent with an isostatic ridge (Figure 5.2), the potential energy of the system implies that the grain configuration at these states is energetically stable. This provides additional evidence that the simple thickness distribution, $g(h)$, is insufficient to describe accurately the mass distribution in deformed floes. While energetically stable, these ridge states are not isostatic according to theory (Roberts and Coauthors 2019) and should be excluded from basin scale sea ice model thickness distributions.

5.2 Simulation Irregularities

Natural pressure ridge formation is a continuous process characterized by many small-scale failures near the convergence point, not recessed back into the colliding floe as it is in the model. This difference is caused by the regularity, and scaling, of the particles in this model. Natural sea ice is characterized by brine inclusions, heterogeneities in the crystal structure, and phase state irregularities. These factors serve to provide weaknesses in the ice that initiate fractures at much lower total strain values than elsewhere in the material. The DEM developed in this thesis, however, does seem to show this continuous failure mechanism once the initial failure has occurred and its associated transient in the system has dispersed.

Figure 5.4 shows the initial failure of the ice floe which is characterized by the formation of a large truss that fails catastrophically to produce the initial ridging region. As the simulation loads stress into the ice floe, elastic deformation forms the truss apparent in Figure 5.4. With continued convergence, the curvature of the truss increases until a critical failure criteria is met and inelastic, brittle failure occurs in the sheet. This catastrophic failure represents a significant departure in the modeled sea ice pressure ridge formation from that found in nature.

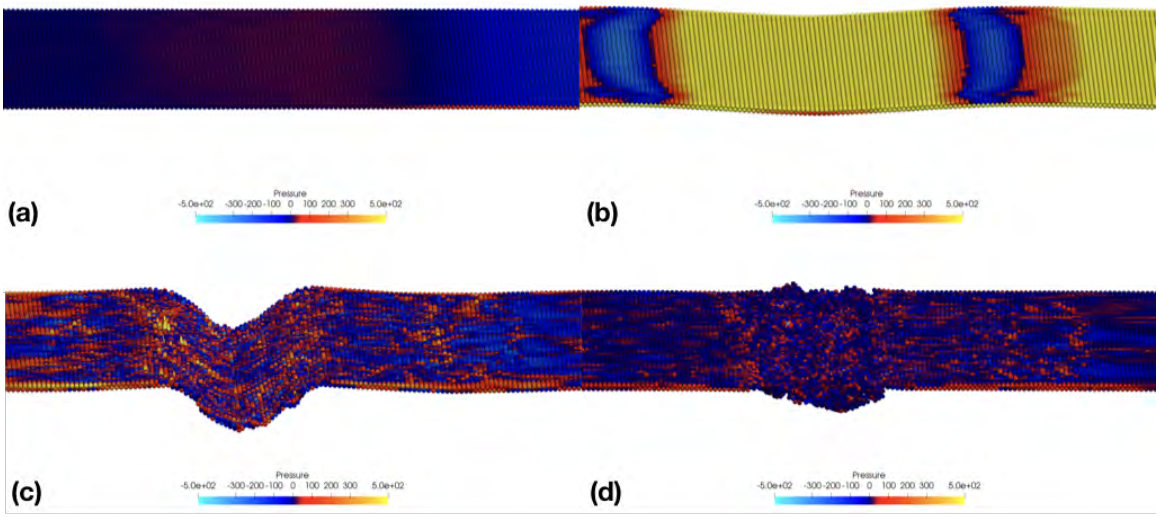

Pictured is the progression of the initial failure. First, the simulation loads (a) where the sheet begins to develop a bending moment evidenced by the focusing of compressive stress at the top of the sheet. With further loading in (b), secondary bending moments to the left and right develop with tension stress bracketing the large compression in the truss system. Finally, (c) shows the transient following the catastrophic failure event when the curvature in the truss system exceeds thresholds. Ultimately, (d) shows shortly after the transient has abated and the system has roughly returned to a hydrostatic configuration.

Figure 5.4. Initial Failure Mode

First, the failure mode is too energetic and removed from the convergence area indicating that the initial failure mode is incorrect. However, once initial failure occurs, the ridge forms within the initial floe consistent with expected behavior. Second, the energetic failure mode creates a severe transient early in the simulation where material is ejected downwards creating an anomalous transient that takes time to dissipate. This source of error is mitigated as the ridge matures and failure is more continuous, generating small amounts of rubble continuously, rather than the large transient apparent at the start of the simulation.

As previously mentioned, the model makes an important assumption of spherical ice particles. This assumption necessitates many of the modifications to the calculation of ϕ_R and affects the dynamics of the formation of the ridge. Furthermore, the simplified grain creates a bond system that does not enforce bond angles. Because of this, some of the material

failures apparent in the system are folds, where the bonds reorient allowing the floe to fold back over on itself, rather than fracture. Inspecting the output, these instances do not appear to impart any large-scale anomalous rubble and does not affect the final computed ridge state.

5.3 Model Refinement

LAMMPS has a number of built in options that are well suited to the generation of large-scale granular systems, like the one presented in this thesis. However, during the development of this model many weaknesses for this particular application were found and further development would ease them for application in the future.

Chief among these deficiencies is the lack of pre-built functions with which to build spatially variable bond structures as well as the ability to break multiple bonds per time step per atom. The first problem was mitigated through external scripting to generate .data files on which LAMMPS populates the simulation. Further refinement to these techniques should enable the creation of more variable bond structures that could serve to mitigate many of the issues present in the previous section. The second of these concerns was mitigated through the use of a bond breaking scheme that checked every ten model steps for bonds that met the failure criteria. This periodicity amounted to quite a few checks per output step, but a more robust solution should be implemented to delete bonds on a more reliable, physical basis.

Finally, research should be done into a more physical bond scheme that incorporates bond strength variability due to the inclusion of sub-grain sea ice variability. The current model iteration only includes minor bond strength variability as a function initial depth in the floe, low values at the bottom of the floe increasing upwards. Extension of this variability to all directions should serve to ease the catastrophic failure and bring low strain ridge formation more in line with natural behavior.

THIS PAGE INTENTIONALLY LEFT BLANK

APPENDIX A:
Timoshenko Cantilever Experiment

This model has been compared to an analytic Timoshenko cantilever solution to assess its ability to simulate a solid material. A virtual cantilever using the same model scheme as the ridge simulator is created. One end of the cantilever is held fast by setting the force on each edge particle to zero. The other end is forced in either the $-\hat{\mathbf{k}}$ or $-\hat{\mathbf{j}}$ direction. The equilibrium displacement as a function of the distance along the cantilever is measured to provide data to generate a Timoshenko solution curve fit and find the effective Elastic Modulus, E.

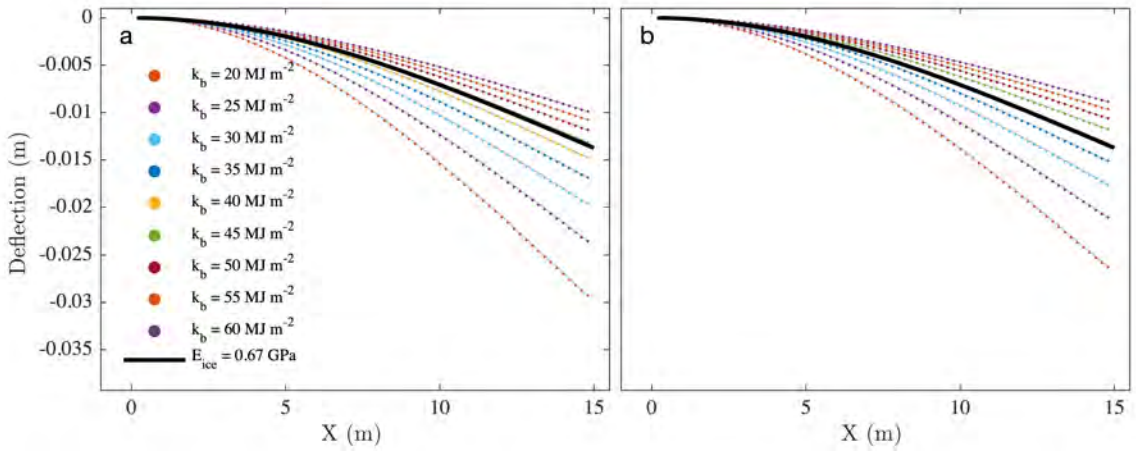

Curve fits applied to mean displacement, $w(x)$, for trials using different values of K_b. For reference, cantilever solutions for $E = 0.67$ GPa are in bold. Point load applied in (a) vertical and (b) horizontal directions. Results are different due to differences in lattice aspect.

Figure A.1. Equilibrium Cantilever Displacement with Constant Point Load

This test was chosen because of the availability of a simple set of equations following the application of Timoshenko Beam Theory presented in Lovell (2002). Consider a beam with length, L, cross section area, A, and second rotational moment, I. In the limit of quasi-static equilibrium with the simple point load applied at x = 0 and the fixed end at x = L, the solution to the displacement of the cantilever, $w(x)$, is

$$w(x) = \frac{P(L-x)}{\kappa AG} - \frac{Px}{2EI}\left(L^2 - \frac{x^2}{3}\right) + \frac{PL^3}{3EI} \tag{A.1}$$

where,

$$\kappa = \frac{10(1+\nu)}{12+11\nu}. \tag{A.2}$$

The results of these trials are presented in Figure A.1. The curve fits are very good indicating that the cantilever behaves as predicted for the geometry and gives reasonably high confidence in the ability of the lattice and bond system to create a material with the same properties as sea ice. Table A.1 summarizes the values obtained and provides the data used to derive a relationship between the bond stiffness and elastic modulus.

Table A.1. Cantilever Bond Stiffness Experiment Summary

K_b (MJ m^{-2})	$E_{y,fit}$ (GPa)	R^2	$E_{z,fit}$ (GPa)	R^2
20	0.347	0.9998	0.311	0.9999
25	0.433	0.9998	0.388	0.9999
30	0.519	0.9998	0.465	0.9999
35	0.605	0.9999	0.542	0.9999
40	0.692	0.9999	0.620	0.9999
45	0.779	0.9999	0.697	0.9999
50	0.866	0.9999	0.775	0.9999
55	0.953	0.9999	0.853	0.9999
60	1.041	0.9999	0.932	0.9999

For material deflected in the $\hat{\mathbf{k}}$ direction, the bond stiffness is,

$$K_b = 0.0577E \tag{A.3}$$

such that the modeled sea ice has the same E as natural sea ice. For deflection in the $\hat{\mathbf{j}}$ direction, the relationship is,

$$K_b = 0.0645E. \tag{A.4}$$

It is assumed that as the size of the particles decrease, this divergence in proportionality constants will abate and the two solutions will converge. This assumption has not been investigated. However, a proportionality constant value of 0.06, the average of the two values, is used to determine the bond stiffness as a function of bond elastic modulus for this model.

THIS PAGE INTENTIONALLY LEFT BLANK

APPENDIX B:
Acoustic Wave Generation

While not investigated in the course of this research, the model seems to be capable of producing interesting acoustic features. Figure B.1 shows the propagation of acoustic energy initiated by the failure of bonds at the left edge. These waves propagate at the sound speed in a material with the same elastic modulus as sea ice. This could enable the simulation of acoustic energy propagation within sea ice that is on the atmosphere/ocean interface. Complex coupling schemes would need to be developed, but this model, at sufficient resolution, seems to be capable of contributing to examination of this problem.

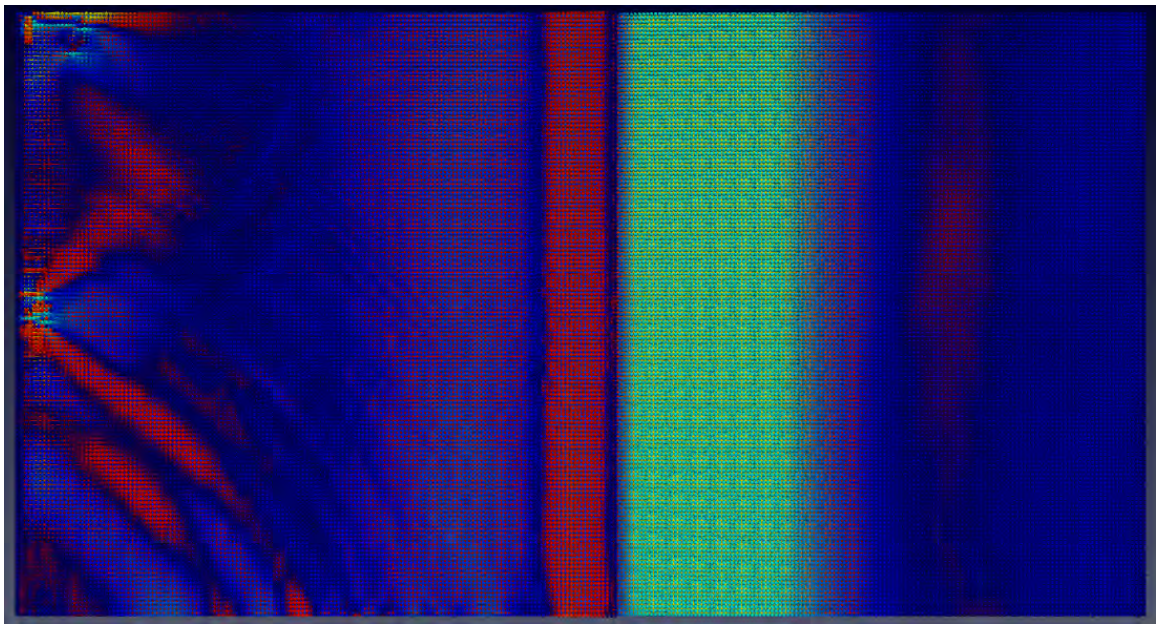

A simulation where the left floe overrides the right floe. The image shows compression, red, and rarefaction, green, in the pressure field. The green region near the center is caused by the elongation of bonds at the top of the subducting floe. At the left, acoustic wave propagation and interference patterns are apparent in the material initiated by bond failures near the moving edge. These pressure waves propagate in the material at the estimated sound speed.

Figure B.1. Acoustic Signal of Failure

THIS PAGE INTENTIONALLY LEFT BLANK

List of References

Brassington, G. B., and Coauthors, 2015: Progress and challenges in short-to medium-range coupled prediction. *J. of Oper. Oceano.*, **8**, doi: 10.1080/1755876X.2015.1049875.

British Broadcasting Corporation, 2014: Denmark challenges Russia and Canada over North Pole. Accessed 22 May 2019, https://www.bbc.com/news/world-europe-30481309.

Cavalieri, D. J., and C. L. Parkinson, 2012: Arctic sea ice variability and trends, 1979-2010. *Cryosphere*, **6 (4)**, 881–889, doi: 10.5194/tc-6-881-2012.

Chief of Naval Operations, USN, 2018: A design for maintaining maritime superiority. URL https://www.navy.mil/navydata/people/cno/Richardson/Resource/Design_2.0.pdf.

Coon, M., and Coauthors, 1974: AIDJEX BULLETIN No. 24: Numerical Modeling Report. 1–106.

Coon, M., R. Kwok, G. Levy, M. Pruis, H. Schreyer, and D. Sulsky, 2007: Arctic Ice Dynamics Joint Experiment (AIDJEX) assumptions revisited and found inadequate. *J. of Geophys. Res.: Oceans*, **112 (11)**, 1–11, doi: 10.1029/2005JC003393.

Davis, N. R., and P. Wadhams, 1995: A statistical analysis of Arctic pressure ridge morphology. *J. Geophys. Res.*, **100 (C6)**, 10 915–10 925, doi: 10.1029/95JC00007.

Davis, T. J., 2019a: Ridge Evolution, Plan View. doi: 10.5281/zenodo.3229206.

Davis, T. J., 2019b: Ridge Evolution, Profile View. doi: 10.5281/zenodo.3229212.

Ekeberg, O., K. Høyland, and E. Hansen, 2015: Ice ridge keel geometry and shape derived from one year of upward looking sonar data in the Fram Strait. *Cold Reg. Sci. Technol.*, **109**, 78–86, doi: 10.1016/j.coldregions.2014.10.003.

Francis, J., and N. Skific, 2015: Evidence linking rapid Arctic warming to mid-latitude weather patterns. *Philosophical Transactions of the Royal Society A: Mathematical, Physical and Engineering Sciences*, **373 (2045)**, 20140 170, doi: 10.1098/rsta.2014.0170, URL http://rsta.royalsocietypublishing.org/lookup/doi/10.1098/rsta.2014.0170.

Garbrecht, T., C. Lüpkes, E. Augstein, and C. Wamser, 1999: Influence of a sea ice ridge on low-level airflow. *J. of Geophys. Res.: Atmospheres*, **104 (D20)**, 24 499–24 507, doi: 10.1029/1999JD900488.

Herman, A., 2016: Discrete-element bonded-particle sea ice model design, version 1.3a - model description and implementation. *Geosci. Model Dev.*, **9 (3)**, 1219–1241, doi: 10.5194/gmd-9-1219-2016.

Hibler, W. D., III, 1979: A dynamic thermodynamic sea ice model. *J. of Geophys. Res.: Oceans*, **9 (4)**, 815–846, doi: 10.1175/1520-0485(1979)009<0815:ADTSIM>2.0.CO;2.

Hibler, W. D., III, 1980: Modeling a variable thickness sea ice cover. *Mon. Weather Rev.*, **108 (12)**, 1943–1973, doi: 10.1175/1520-0493(1980)108$<$1943:MAVTSI$>$2.0.CO;2.

Hopkins, M. A., 1994: On the ridging of intact lead ice. *J. of Geophys. Res.*, **99 (C8)**, 16 351, doi: 10.1029/94JC00996.

Hopkins, M. A., 1998: Four stages of pressure ridging. *J. of Geophys. Res.: Oceans*, **103 (C10)**, 21 883–21 891, doi: 10.1029/98JC01257.

Hutchings, J., P. Heil, and W. D. Hibler, III, 2009: Modeling linear kinematic features in pack ice. *J. of Geophys. Res.: Oceans*, **114 (12)**, 3481–3497, doi: 10.1029/2008JC005217.

Johnston, M., and A. Barker, 2000: Microstructure of first year sea ice ridges. Tech. Rep. HYD-TR-043, Canadian Hydraulics Center, 58 pp. doi: 10.4224/12340979.

Kramer, A. E., 2016: Russia Presents Revised Claim of Arctic Territory to the United Nations. The New York Times, Accessed 22 May 2019, https://www.nytimes.com/2016/02/10/world/europe/russia-to-present-revised-claim-of-arctic-territory-to-the-united-nations.html.

Kwok, R., and G. F. Cunningham, 2008: ICESat over Arctic sea ice: Estimation of snow depth and ice thickness. *J. of Geophys. Res.*, **113**, 1–17, doi: https://doi.org/10.1029/2008JC004753.

LAMMPS, 2017: LAMMPS Users Manual. URL http://lammps.sandia.gov, 2004 pp., doi: 10.1002/ejoc.201200111, arXiv:1011.1669v3.

Lipscomb, W. H., and Coauthors, 2007: Ridging, strength, and stability in high-resolution sea ice models. *J. of Geophys. Res.: Oceans*, **112 (C3)**, doi: 10.1029/2005JC003355.

Lovell, E. G., 2002: *Solid mechanics: a variational approach*, Vol. 298. 468 pp., doi: 10.1016/0016-0032(75)90062-9.

Melia, N., K. Haines, and E. Hawkins, 2016: Sea ice decline and 21st century trans-arctic shipping routes. *Geophys. Res. Letters*, **43 (18)**, 9720–9728, doi: 10.1002/2016GL069315.

Melling, H., and D. A. Riedel, 1995: The Underside Topography of Sea-Ice over the Continental-Shelf of the Beaufort Sea in the Winter of 1990. *J. Geophys. Res.*, **100 (C7)**, 13 641–13 653.

Melling, H., and D. A. Riedel, 1996: Development of seasonal pack ice in the beaufort sea during the winter of 1991-1992: A view from below. *J. of Geophys. Res.: Oceans*, **101 (C5)**, 11 975–11 991, doi: 10.1029/96JC00284.

Melling, H., D. R. Topham, and D. Riedel, 1993: Topography of the upper and lower surfaces of 10 hectares of deformed sea ice. *Cold Reg. Sci. Technol.*, **21 (4)**, 349–369, doi: 10.1016/0165-232X(93)90012-W.

Parmerter, R. R., and Coauthors, 1972: Model of pressure ridge formation in sea ice. *J. of Geophys. Res.*, **77 (33)**, 6565–6575, doi: 10.1029/JC077i033p06565.

Perovich, D. K., and J. A. Richter-Menge, 2009: Loss of sea ice in the arctic. *Ann. Rev. of Marine Sci.*, **1 (1)**, 417–441, doi: 10.1146/annurev.marine.010908.163805.

Plimpton, S., 1995: Fast parallel algorithms for short-range molecular dynamics. *J. of Comp. Phys.*, **117 (1)**, 1–19, doi: https://doi.org/10.1006/jcph.1995.1039.

Roberts, A. F., and Coauthors, 2019: A variational method for sea ice ridging in earth system models. *J. of Advances in Modeling Earth Systems*, **11**, 771–805, doi: 10.1029/2018MS001395.

Rothrock, D. A., 1975: The energetics of the plastic deformation of pack ice by ridging. *J. Geophys. Res.*, **80 (33)**, 4514–4519, doi: 10.1029/JC080i033p04514.

Secretary of Defense, 2018: Summary of the 2018 National Defense Strategy of the United States of America. Accessed 22 May 2019, https://dod.defense.gov/Portals/1/Documents/pubs/2018-National-Defense-Strategy-Summary.pdf.

SEDNA, 2008: *The Sea Ice Experiment: Dynamic Nature of the Arctic, Applied Physics Laboratory Ice Station 2007, Field Report, J. Hutchings ed.* 145 pp.

Shea, N., 2019: Scenes from the new Cold War unfolding at the top of the world. National Geographic, Accessed 14 May 2019, https://www.nationalgeographic.com/environment/2018/10/new-cold-war-brews-as-arctic-ice-melts/.

Silbert, L. E., and Coauthors, 2001: Granular flow down an inclined plane: Bagnold scaling and rheology. *Phys. Rev. E*, **64**, doi: 10.1103/PhysRevE.64.051302.

Strub-Klein, L., and D. Sudom, 2012: A comprehensive analysis of the morphology of first-year sea ice ridges. *Cold Reg. Sci. Technol.*, **82**, 94–109, doi: 10.1016/j.coldregions.2012.05.014.

Tan, B., and Coauthors, 2012: Morphology of sea ice pressure ridges in the northwestern Weddell Sea in winter. *J. Geophys. Res. Ocean.*, **117 (6)**, 1–13, doi: 10.1029/2011JC007800.

Thorndike, A. S., and Coauthors, 1975: The thickness distribution of sea ice. *J. of Geophys. Res.*, **80 (33)**, 4501–4513, doi: 10.1029/JC080i033p04501.

Timco, G., and R. Burden, 1997: An analysis of the shapes of sea ice ridges. *Cold Reg. Sci. Technol.*, **25**, 65–77, doi: 10.1016/S0165-232X(96)00017-1.

Timco, G., K. Croasdale, and B. Wright, 2000: An Overview of First-Year Sea Ice Ridges. Tech. rep., 157 pp.

Tsamados, M., and Coauthors, 2014: Impact of variable atmospheric and oceanic form drag on simulations of arctic sea ice. *J. of Phys. Oceano.*, **44 (5)**, 1329–1353, doi: 10.1175/JPO-D-13-0215.1.

Tsamados, M., D. L. Feltham, and A. V. Wilchinsky, 2013: Impact of a new anisotropic rheology on simulations of arctic sea ice. *J. of Geophys. Res.: Oceans*, **118 (1)**, 91–107, doi: 10.1029/2012JC007990.

Tucker, W. B., III, and J. W. Govoni, 1981: Morphological investigations of first-year sea ice pressure ridge sails. *Cold Reg. Sci. Technol.*, **5 (1)**, 1–12.

Wadhams, P., and T. Davy, 1986: On the spacing and draft distributions for pressure ridge keels. *J. Geophys. Res.*, **91 (C9)**, 10 697, doi: 10.1029/JC091iC09p10697.

Weeks, W. F., 2010: *On Sea Ice*. University of Alaska Press, 664 pp.

Wen, P., 2019: China unveils vision for 'Polar Silk Road' across Arctic. Reuters, Accessed 22 May 2019, https://www.reuters.com/article/us-china-arctic/china-unveils-vision-for-polar-silk-road-across-arctic-idUSKBN1FF0J8.

Wilchinsky, A., D. L. Feltham, and M. A. Hopkins, 2011: Modelling the reorientation of sea-ice faults as the wind changes direction. *Annals of Glaciology*, **52 (57 PART 1)**, 83–90, doi: 10.3189/172756411795931831.

Zhang, H. P., and H. A. Makse, 2005: Jamming transition in emulsions and granular materials. *Phys. Rev. - Statistical, Nonlinear, and Soft Matter Physics*, **72 (1)**, 1–12, doi: 10.1103/PhysRevE.72.011301.

Zubov, N. N., 1945: *L'dy Arktiki*. Izdatel'stvo Glavsevmorputi, Moscow, Russia (1963 English translation 'Arctic Ice' by U.S. Navy Electronics Laboratory, San Diego, California, USA, 510pp), 491 pp.

Initial Distribution List

1. Defense Technical Information Center
   Ft. Belvoir, Virginia

2. Dudley Knox Library
   Naval Postgraduate School
   Monterey, California